7-1-2016

Characterization of Consolidated Granular Salt

Melissa Marie Mills

Melissa Marie Mills

Candidate

Civil Engineering

Department

This thesis is approved, and it is acceptable in quality and form for publication:

Approved by the Thesis Committee:

Dr. John C. Stormont, Chairperson

Dr. Bruce M. Thomson, Member

Dr. Frank D. Hansen, Member

Dr. Stephen J. Bauer, Member

CHARACTERIZATION OF CONSOLIDATED GRANULAR SALT

by

MELISSA MARIE MILLS
B.Sc. Civil Engineering, University of New Mexico, 2013
M.Sc. Civil Engineering, University of New Mexico, 2016

THESIS

Submitted in Partial Fulfillment of the

Requirements for the Degree of

Master of Science

Civil Engineering

The University of New Mexico

Albuquerque, New Mexico

July 2016

CHARACTERIZATION OF CONSOLIDATED GRANULAR SALT

by Melissa Marie Mills
B.Sc. Civil Engineering, University of New Mexico, 2013
M.Sc. Civil Engineering, University of New Mexico, 2016

ABSTRACT

Granular salt is likely to be used as backfill material and a seal system component within geologic salt formations serving as a repository for long-term isolation of nuclear waste. Pressure from closure of the surrounding salt formation will promote consolidation of granular salt, eventually resulting in properties comparable to native salt. Understanding the consolidation processes dependence on stress state, moisture availability, and temperature is important for demonstrating sealing functions and long-term repository performance. This study includes the characterization of laboratory-consolidated salt by means of microstructural observations, measurement of physical properties related to the pore structure, and quantification of pore sizes areas under differing conditions. Samples for this study were obtained from mine-run granular salt from the Waste Isolation Pilot Plant (WIPP) and Avery Island which were consolidated hydrostatically with varying conditions of stress up to 38 MPa, temperatures up to 250°C, and moisture additions of 1%. Porosities achieved from consolidation ranged between 0.01 and 0.22.

Microstructural observations using optical and scanning electron (SEM) microscopes were made to provide direct insight into deformation mechanisms during consolidation.

Porosity, specific surface area, permeability, and tortuosity factor were quantified through multiple techniques including point counting, petrographic image analysis (PIA), porosimetry, and steady-state gas permeametry. Pore area distributions categorized into micropores (<1000 μm^2) and macropores (>1000 μm^2) were developed from Back-Scattered Electrons (BSE) SEM images analyzed in *Fiji*. .

Overall, the addition of moisture produces a higher degree of cohesion among grains, lower permeabilities and porosities as well as higher specific surface areas and lower macropore frequency at higher temperatures. A higher stress was also seen to lower porosity, increase specific surface area, and lower the frequency of micropores. Higher temperature samples experienced low porosities, more grain boundary cohesion, and, in WIPP samples, a higher frequency of macropores in the range from 1000 to 2500 μm^2. From microstructural observations, samples with 1% added moisture or those which were unvented during consolidation demonstrated clear pressure solution processes with tightly cohered grain boundaries and areas of occluded fluid pore spaces. Samples consolidated without additional moisture exhibited mainly cataclastic and plastic deformation. Recrystallization was also observed in samples consolidated at temperatures of 90°C with added moisture and 250°C. Porosities obtained from methods that measured both total and connected porosity were similar, suggesting a connected pore network within samples. From image analysis, a general trend of increase in specific surface area with a decrease in porosity was observed. Permeability values decreased with decreasing porosity and are comparable to permeability-porosity relationships for rock salt published by others. The tortuosity factor was calculated from

the Carman-Kozeny model, which incorporates permeability, porosity, and specific surface area, and generally increased with decreasing porosity. Pore area analysis reveals porosities consisting predominately of macropores and minor changes in pore area frequencies with respect to consolidation conditions.

It is well known that stress, temperature, and moisture affect the behavior of salt consolidation, but complete studies on deformation mechanisms and the evolving pore structure over a large range of conditions is not abundant. Information provided here enhances the current understanding of granular salt consolidation by offering direct insight into micro-mechanic processes and transformation of pore structure components.

TABLE OF CONTENTS

1. INTRODUCTION

1.1. BACKGROUND

Rock salt is a viable geologic repository host for disposal of waste from nuclear energy and nuclear weapon by-products, due to its location in stable geologic areas, plastic material behavior, and low permeability (Winterle et al., 2012). Disposal in rock salt is being used and/or considered at numerous locations throughout the world such as the Waste Isolation Pilot Plant (WIPP) in the USA, and the Asse II and Morsleben mines in Germany. After waste has been placed, granular salt is likely to be used as back-fill material for mined tunnels and shafts to completely encase waste. It is expected that granular salt will eventually consolidate to a condition comparable to the host rock, which is why understanding deformation mechanisms and pore structure evolution as granular salt consolidates is key for determining long-term repository performance for complete isolation.

Consolidation is essentially pore volume reduction, where the amount and nature of the final pore volume is dependent on a multitude of factors. Consolidation of granular salt is mainly a function of stress, temperature, and moisture conditions, but also time and impurity (e.g., clay) amounts. As granular salt consolidates, the initial void reduction is due to brittle processes of grain rearrangement and cataclastic flow. Eventually, grain boundary processes and crystal-plastic mechanisms, which include deformation mechanisms, control additional porosity reduction. Deformation mechanisms that occur

simultaneously with increasing temperature and stress include dislocation multiplication, glide, cross slip, climb, fluid-assisted creep, and annealing/recrystallization.

Deformation mechanisms have been widely studied through microstructural observations by a variety of authors (e.g. Urai et al., 1986a, 1986b; Spiers and Brzesowsky, 1993; Hansen et al., 2012; Broome et al., 2014). Dislocations are defects in a crystal structure, where any applied stress immediately increases dislocation densities making dislocation multiplication a preliminary, transient deformation mechanism observed in natural rock salt by Carter et al. (1982), Urai et al. (1986), and Hunsche and Hampel (1999), among others. This process creates a lattice distortion leading to strain hardening from obstructed movement when other mechanisms are unable to transport dislocations. The movement of dislocations can occur by glide, a plastic deformation process, also known as slip in material science terms. With glide, dislocations move along a family of crystallographic planes with shear stresses that exceed the critical resolved shear stress. This movement produces glide bands, which highlight primary slip systems in minerals (Carter and Heard, 1970). When barriers exist in the crystal lattice, glide is aided by the dynamic recovery processes of cross slip and climb, as seen by Senseny et al. (1992). Cross slip is apparent at low temperatures and involves screw dislocation movements from one glide plane to another with the same Burger's vector. In another direction, climb occurs as dislocations move perpendicular to the glide plane at higher temperatures. When rock salt includes small amounts of moisture, solution precipitation processes, such as fluid-assisted creep, help reduce dislocation densities and influence grain boundary migration leading to recrystallization (Urai and Spiers, 2007). Fluid-

assisted creep, or the more commonly identified earth science term pressure solution, comprises of the transfer of fluid along grain boundaries where portions of highly stressed grains dissolve owing to increased solubility and precipitate at lower stress interfaces. Fluid-assisted migration is capable of removing stored energy even at ambient temperatures and therefore noticeably accelerates the densification of granular salt (Spiers et al., 1990; Callahan et al, 1996, 1998). Annealing/recrystallization is the ultimate recovery process that is thermally activated and involves strain softening when work-hardening processes are unbalanced. Recrystallization has been rarely observed in rock salt consolidation experiments (Carter et al., 1982; Urai et al., 1986b, Hansen et al., 2012) because of the limited test duration and conditions (e.g., temperature, added moisture, etc.), and/or excluded observational work altogether. Recrystallization has been more frequently observed in naturally deformed salt studies (Debois et al., 2010; Schleder and Urai, 2005)

A small change in temperature, stress, or moisture availability during consolidation can greatly influence the deformation mechanisms that take place. Rock salt consolidated at lower temperatures with dry conditions at high stresses tends to experience mainly cataclastic fracture processes or grain sliding, evident by dislocation multiplication and glide mechanisms. Broome et al. (2014) observed that at higher temperatures, effective porosity is lowered and extensive glide enables grain deformation along with thermally activated climb recovery. This led to fluid inclusions moving to grain boundaries where consolidation continues by plasticity-aided pressure solution processes. Added moisture in synthetic salt has shown rapid recrystallization at grain boundaries from fluid-assisted

creep (Urai and Spiers, 2007); however, there have been few (e.g., Urai et al., 1986b; Brodsky et al., 1996) microstructural observations on consolidation of natural granular rock salt with an amount of water added consistent with field operational plans; that is, less than saturated.

Understanding the evolving pore structure under different consolidation conditions is critical for assessing how transport properties will change. Of particular interest are the conditions that lead to a very low permeability when the granular salt will become an effective seal material. The pore structure in consolidating granular salt can be characterized by its amount (porosity), distribution of pore areas, and connectivity. Keller et al. (2014) examined the macro (radii > 4 μm) and micro-pores (radii < 1 μm) of oedometer tested crushed rock salt with different degrees of compaction at temperatures of 100°C and 200°C. Their pore space dimensions were defined by incompatibilities between angular grains and grain aggregates. By using X-ray computer tomography and Focused Ion Beam nanotomography, 3D reconstructions were evaluated for homogeneity, percolation properties, pore size distribution, and connectivity of the pore space. It was found that the 200°C sample had lower porosity, connectivity, macro-porosity, average pore size radii, and a higher percolation threshold (0.08-0.14) in terms of macro-porosity when compared to the 100°C sample. It was also found that the micropores mainly lie along grain boundaries with poor connectivity and are related to fluid inclusion formation based on their pore geometry.

Pore structure can also be significantly influenced by the availability of moisture as summarized in Hansen et al. (2014). The topology of fluid in granular salt is controlled by the dihedral angle θ, which is a balance of solid-solid and solid-fluid interfacial energies, and allows for an interconnected network of fluid at triple grain boundaries when less than 60°. When greater than 60°, fluid is restricted to isolated pores along grain boundaries and/or triple junctions. As granular salt is consolidated, the main pore space fluid is compressed and forced out of the consolidating mass until there is little connected porosity. At this stage, the saturation of the intergranular pore space increases and further fluid transport involves two-phase flow of trapped air and brine.

While there are many experimental methods to acquire pore characteristics, petrographic image analysis (PIA) is a rapid way to quantify petrophysical properties. PIA analyzes microscopic images from rock thin sections ascertain quantitative measurements of porosity, pore shape, area, and specific surface area. From this technique, two-dimensional parameters are obtained and used to describe three-dimensional properties of porous media (Mowers and Budd, 1996). Cerepi et al. (2001) used PIA to quantify the pore space of carbonate rocks by segmented, binary images from backscatter scanning electron (BSE) and optical microscopes. The pore space was divided into macro and micro porosity where petrophysical image parameters based on stereologic principles were used to find image porosity, specific surface area, and pore throat size relating to capillary pressure. When compared to classic petrophysical methods such as mercury injection porosimetry, it was found that image porosity and surface area were lower than mercury injection techniques. They found this to be because of their image analysis

techniques, which could only measure pore throat sizes of 0.03 μm and greater, whereas pore sizes as small as 0.005 μm were resolved with mercury injection. Mowers and Budd (1996) found that micropores unresolved by PIA did not greatly influence permeability.

A principal consequence of a pore volume reduction by consolidation is a decrease in permeability. Permeability measurements have been made on granular and synthetic salt under a variety of stress, temperature, and moisture conditions (Holcomb and Shields, 1987; Case et al., 1987; Brodsky, 1994; Cinar et al., 2006; Stührenberg and Schulze, 2012; Bauer et al., 2015). Results have been previously described by a power-law, i.e., $k \sim \phi^x$, with an exponent in the 4 to 5 range (Cinar, 2006; Blanco Martin et al., 2015; Hansen et al., 2015). At low porosities (<0.05), there is an indication that the permeability decreases at an accelerated rate with respect to porosity. Stormont et al. (2015) suggested the permeability-porosity behavior of granular salt was similar to that which has been observed for other materials, including calcite, quartz, and sandstone (e.g., Zhu et al., 1995). Above some critical porosity, the porosity remains largely connected and involved in the flow and can be described by a power law relation. Below the critical porosity, which has been estimated in the range of 0.02 and 0.05 (Stormont et al., 2015), pore connectivity is progressively lost and the permeability decrease accelerates. Eventually, below a percolation threshold, any remaining pores become completely isolated and there is no measureable permeability.

An important observation from previous permeability studies is the role of water in reducing the permeability of granular salt. Brodsky (1994) found that even at a relatively

low confining pressure (6.9 MPa) and temperature (25°C), samples with added moisture (3% by weight and saturated) consolidated to high fractional densities (>0.90) yielding permeabilities below 6 x 10^{-18} m^2. Stührenberg and Schulze (2012) also concluded that wet consolidation conditions greatly reduce permeability: at modest consolidation conditions (20 MPa and 22°C), the permeability of consolidated salt was less than 1 x 10^{-20} m^2, whereas at dry conditions, consolidation at elevated conditions (38 MPa and 100°C) only reduced the permeability to 1 x 10^{-16} m^2. Popp et al. (2013) demonstrated that when consolidation involves pressure solution mechanism due to available moisture, the permeability is lower than comparable deformation by other mechanisms. These results indicate that the pressure solution mechanism effectively reduces the conductivity of the pore structure along grain boundaries and contacts. Cinar et al. (2006) noted that adding too much water may be problematic as saturated conditions can increase pore pressure, which decreases effective consolidation stresses, and may result in a relatively large residual porosity and permeability.

Consolidation of natural granular rock salt has been widely studied (Holcomb and Shields, 1987; Case et al., 1987; Brodsky, 1994; Hunsche and Hampel, 1999; Stührenberg and Schulze, 2012; Bauer et al., 2015) with the main focus on mechanical responses and some microstructural observations, but limited emphasis on pressure solution processes and pore structure parameters (e.g., specific surface area, pore size, tortuosity, etc.). Pressure solution processes and pore structure parameters have primarily been investigated by consolidation or compaction experiments on synthetic salt, such as table salt or analytical grade NaCl granulates, used as a reference material to natural

granular rock salt (Spiers and Brzesowsky, 1993; Cinar et al., 2006; Urai and Spiers, 2007; Pennock et al., 2007; Zhu et al., 2015). For instance, Spiers and Brzesowsky (1993) studied dry and brine-saturated NaCl granulates under conditions of axial stresses up to 8MPa and ambient temperature, resulting in porosities between 0.17 and 0.3. They observed clear evidence of densification by pressure solution processes and lower porosities in brine-saturated samples. Cinar et al. (2006) also consolidated NaCl granulates at ambient temperature, but higher stresses from 50 to 150 MPa and an added water content of 0.3%, obtaining porosities from 0.025 to 0.05. While values for pore throat radius, specific surface area, and tortuosity were found, no microstructural observations were made. Image analysis methods were studied in Zhu et al. (2015) on small compacted table salt samples to examine the evolution of porosity by measuring the change in position of void centroids over time. Conditions were focused for stresses up to 0.5 MPa at ambient temperatures and dry conditions (restricting pressure solution processes) and an average porosity of 0.18 was reported on one sample image divided into six sections after 92 days.

1.2. OBJECTIVES

Although the experiments presented here provide insight into the behavior of salt during consolidation, the incorporation of micro-mechanic observations together with petrophysical measurements and pore structure characterization of natural granular salt at low porosities have not been established. A principal objective of this work is to document the relationship between deformation mechanisms that occur in granular salt and the varying consolidation conditions. Pressure solution processes are emphasized due

to the significant effects on reducing stored energy within grains, which in turn enhances densification and lowers permeability. Another objective of this work is to quantify how pore structure changes with consolidation under different conditions through measurement of physical properties and image analyses of pores. Permeability measurements are used to relate the transport properties and pore structure of granular salt. An important application of this work may be in informing the development and parameterization of constitutive models for granular salt consolidation.

2. MATERIALS AND METHODS

2.1. CONSOLIDATION EXPERIMENTS

Mine-run granular salt from WIPP, located in a bedded salt formation, and the Avery Island mine, located in a domal salt formation, was consolidated in laboratory hydrostatic creep tests with temperatures up to 250°C and confining pressures up to 38 MPa, shown in Table 1. The granular salt was screened to exclude particles larger than 9.5 mm and dried at 110°C. To produce material for wetted samples, granular salt was spread out in trays in a single layer and exposed to 100% humidity conditions until 1% moisture content by weight was achieved. Domal formations can have arguably up to 1% natural water content, where bedded can contain up to 3-5% depending on impurity contents (Hunsche and Schulze, 2002; Kuhlmann, 2014). Cylindrical samples (Figure 1), nominally 105 mm diameter and 122 mm tall, were created by placing the prepared granular salt into copper and malleable soldered lead tubes fitted with end caps. The jacketed samples, which had an initial porosity of about 0.30, were placed in a pressure vessel within a load frame. Band heaters on the pressure vessel were used to achieve and maintain the test temperature. Hydrostatic stresses on the sample were generated by pressurizing the hydraulic oil in the pressure vessel. Stress and strain were monitored during consolidation by monitoring axial displacement with LVDTs, lateral displacements with Schuler gages, and confining fluid volume and pressure. In some tests, concurrent gas permeability measurements were made during consolidation. Test durations ranged from a few days to a few months. Final fractional densities were between .9 and 1.0. A more complete description of the consolidation tests can be found in Bauer et al. (2015) and Broome et al. (2014). At the conclusion of the consolidation

test, sub-samples derived from the consolidated samples were subjected to permeability and porosity measurements, thermal properties measurements, and microstructural observations.

Table 1: Consolidated samples with associated conditions. In sample names, "W" represents WIPP salt and "A" represents Avery Island salt, where 90, 175, and 250 are respective temperatures in °C. *Preconsolidated implies only confining pressure applied without contact from an axial piston.

Sample Name	Temperature (°C)	Hydrostatic Stress (MPa)	Moisture Added	Elapsed Consolidation Time (Days)
W90-1	90	20	None	111
W90-2	90	20	1%	16
W90-3	90	20	1%	1 (Preconsolidated*)
W90-4	90	20	1%	5
W90-7	90	20	1%	23
W90-8	90	38	None	8
W175-1	175	20	None	3
W250-1	250	20	None	14
W250-2	250	20	None, Unvented	12
A250-1	250	20	No	7
A250-2	250	20	1%	7

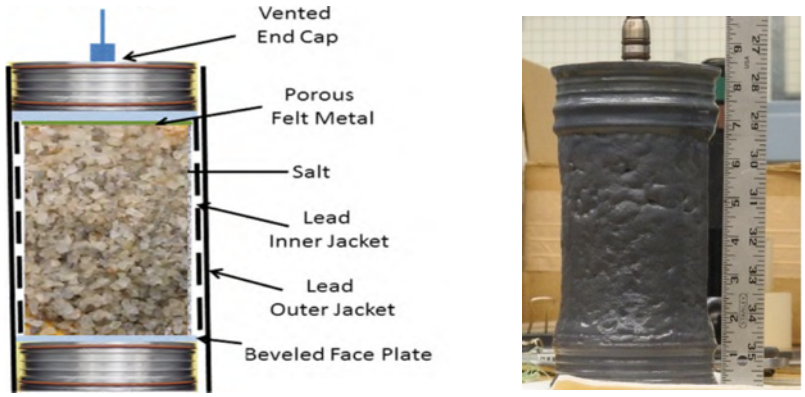

a. b.

Figure 1: a. Example of sample assemblage for consolidation. b. Sample after consolidation.

2.2. MICROSCOPIC OBSERVATIONAL METHODS

Observational techniques were used on consolidated and in-situ samples to gain insight into deformation mechanisms and resulting pore structure. In order to perform numerous types of observations, multiple samples were produced from both deformed and native salt. They comprise of polished thick petrographic sections, cleavage chips, and freshly broken surfaces. Ends of consolidated samples were cut with a diamond wire saw to minimize damage and create sub-samples. A number of sub-samples were commercially vacuum impregnated with blue stained RF 1366 resin and thin sectioned, while others were vacuum impregnated with rhodamine-B doped Spurr Low-Viscosity resin and cut using a Buehler IsoMet slow speed saw. Fresh aggregate fragments were carefully broken from sub-samples by hand to expose clean surfaces that exhibit sample cohesiveness, grain boundary characteristics, and other evidence of micro-processes. Observational devices include optical and scanning electron microscopes (SEM). A Leitz Ortholux II optical microscope equipped with a Leica camera and Leica Application Suite software was used to examine unetched/etched cleaved chips and thin sections, point count, and capture images. Three SEM's (JEOL 5800LV, FEI Nova 200 Nanolab, Tescan Vega3 LM) were used to view Au-Pd coated etched thin sections, etched cleavage chips, and freshly broken aggregate surfaces. Etching highlights grain microstructure and is completed using a solution of methanol saturated with $PbCl_2$ as the etchant followed by transferring to butanol to stop the etch. Point counting on thin sections is a standard technique of optical microscopy and was done to manually determine the porosity of a sample. This consists of counting the number of void spaces and solid spaces in a grid-like pattern for a minimum of 300 counts.

2.3. IMAGE ANALYSIS

The open software package *Fiji* (Schindelin et al., 2012) was used to process images and develop pore area distributions. Thin sections were imaged under BSE-SEM in wide field view at resolutions down to 0.37 μm/pixel to capture pore structure for processing in *Fiji*. An example of the process is given in Figure 2. The threshold of each image was adjusted to contrast pore space (white) and grains (black), which was then analyzed by the *Analyze Particle* function in *Fiji*, omitting pixel areas less than 10 μm^2 to reduce noisy results.

a. b. c.

Figure 2: a. Original BSE-SEM image. b. Threshold of image adjusted with white pore space and black grain space. c. Generated outline of counted pores after particles were analyzed.

Four images were taken at different locations from each sample thin section to process in *Fiji*. Pore area and perimeter were obtained from analysis, and used to calculate porosity (φ), specific surface area (SA), and pore area distributions. For image porosity, resulting pore area was summed and divided by the image area. Specific surface area was calculated by the following relationship (Cerepi et al., 2001):

$$SA = \frac{4\sum_{i=1}^{n} P_i}{\pi \sum_{i=1}^{n} A_i} \qquad (1)$$

where P_i is the perimeter of pore i, A_i is the area of pore i, and n is the total number of analyzed pores. This relationship assumes the projection of a convex shape (Underwood, 1980). To confirm the accuracy of four images, ten images were taken in a grid-like pattern on one sample, and measurements of porosity and specific surface area were obtained. The porosity and specific surface area derived from ten images were within 7% and 5% of the porosity and specific surface area, respectively, derived from four images.

2.4. SUB-CORE PERMEABILITY MEASUREMENTS

Cylindrical ends were cored to obtain 25.4 mm diameter sub-samples used for porosity and permeability measurements. Sub-cores were jacketed in a UV cure coating with appropriate end caps and placed into a silicon oil confining pressure vessel. A confining pressure of 0.689 MPa (100 psi) was applied. By means of the gas lines that penetrated the pressure vessel and connected to the end caps, pressurized nitrogen was supplied to one end of the sample while the other end vented to atmospheric pressure. The flowrate was measured with flowmeters that were calibrated to acquire flowrates from 0.5 to 4000 standard cubic centimeters per minute. Three upstream pressures of 0.138, 0.241, and 0.345 MPa (20, 35, and 50 psi) were used for each sub-core. After a constant flowrate developed at each pressure, as indicated by a change of less than 5%, flow continued for at least fifteen minutes, where a data point was collected every minute. Permeability *k* was calculated by the following:

$$k = \frac{2q\mu L}{A}\frac{P_a}{P^2 - P_a^2} \qquad (2)$$

where q is the flow rate (standard volumetric flow), A is the sample cross sectional area, L is the sample length, μ is the gas viscosity, P_a is atmospheric pressure, and P is the inlet

pressure. The interpreted permeability obtained at the three upstream pressures were used to derive the gas slip or Klinkenberg correction (Peters, 2012). This correction consisted of plotting calculated permeability values vs the inverse mean pore pressure with a best fit line, where the intercept is the intrinsic gas permeability at infinite pressure.

3. RESULTS AND DISCUSSION

3.1 DEFORMATION MECHANISMS

Thin sections and broken aggregate samples expose deformation mechanisms taking place during consolidation experiments varying in pressure, temperature, and moisture conditions. Photomicrographs from freshly broken aggregate pieces examined under the SEM are shown in Figure 3. In can be seen that samples without added 1% moisture at temperatures of 90°C and 175°C (a.-c.) have copious amounts of mechanically ground surfaces and plastic processes occurring. Figures 3a. and b. were imaged at a magnification of 500x and show mainly abraded surfaces with evidence of some pore space. Figure 3c. is a high magnification (1,300x) photomicrograph of a sample consolidated at a higher temperature. In this image, plastic deformation is observed with the lower grain pushing up against the upper grain, generating stresses and causing the crystal (110) dodecahedron planes within the upper grain to distort (see annotations).

Samples with 1% added moisture (Figure 3d.-k. and p.) appear to have a higher level of cohesion at grain boundaries resulting in more cleaved surfaces, which are created by breaking through the crystal structure, and more instances of pressure solution processes. Figures 3e., f., i., j., and k. are all examples of pressure solution processes occurring at grain boundaries. They reveal rounded cubic grains creating a sharp, yet cohered deformation within adjacent grains. Figure 3k. shows ubiquitous rounded cubic grains, indicating pressure solution, with multiple grain boundaries that are tightly cohesive. The only evident void space is represented by isolated and occluded fluid pore spaces found along grain boundaries (noted with arrows). These inhomogeneous features, formed

during deformation, were found among the 1% added moisture and unvented samples displayed prominently in Figures 3d., g., h., m., and n. Between magnifications of 500x to 1,500x, arrays of droplets and canals of residual moisture are apparent along grain boundaries. Similar results were found on deformed Asse mine samples in Urai et al. (1986b) and on WIPP salt with 1% added moisture in Brodsky et al. (1996). The unvented sample, W250-2 (Figure 3m. and n.), retained all natural moisture creating isolated and occluded fluid pore space while promoting fluid aided processes and achieving a high degree of consolidation. However, the vented sample with the same consolidation parameters (W250-1), also experienced a high degree of consolidation evident by tight grain boundaries and cleaved surfaces even when steam, from natural fluid, was observed escaping the sample during consolidation. These results suggest that consolidation at 250°C proceeds relatively rapidly whether or not there was additional moisture. Figure 3o. is a natural Avery Island sample without 1% moisture added showing an evidently tight grain boundary, but mainly abraded surfaces, implying the grains were not completely fused together. A sample with 1% added moisture (Figure 3p.), a cleaved grain surface is observed on the upper grain, indicating a break through the crystal structure and more cohesion at the grain boundary.

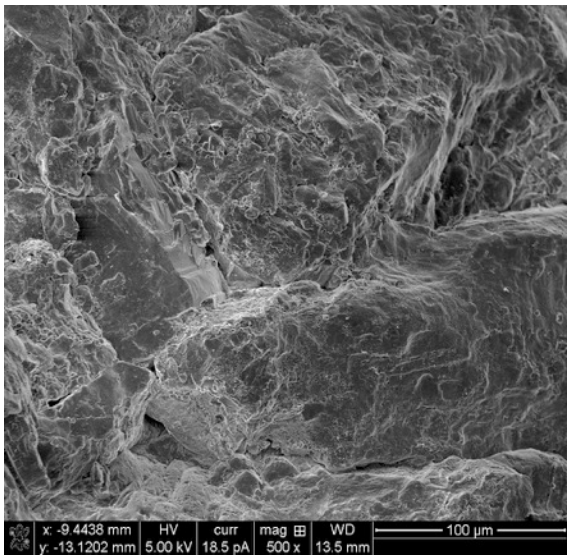

a. W90-1

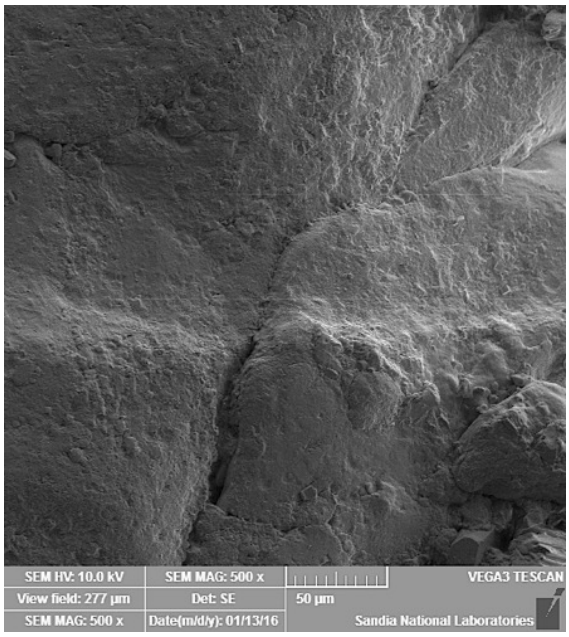

b. W90-8

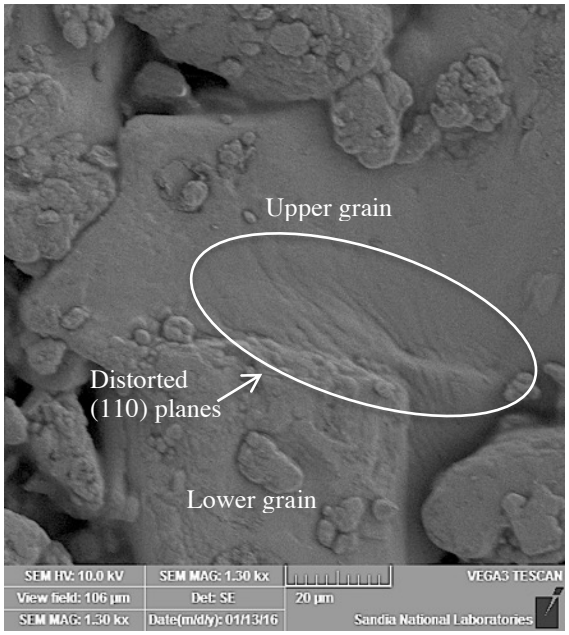

c. W175-1

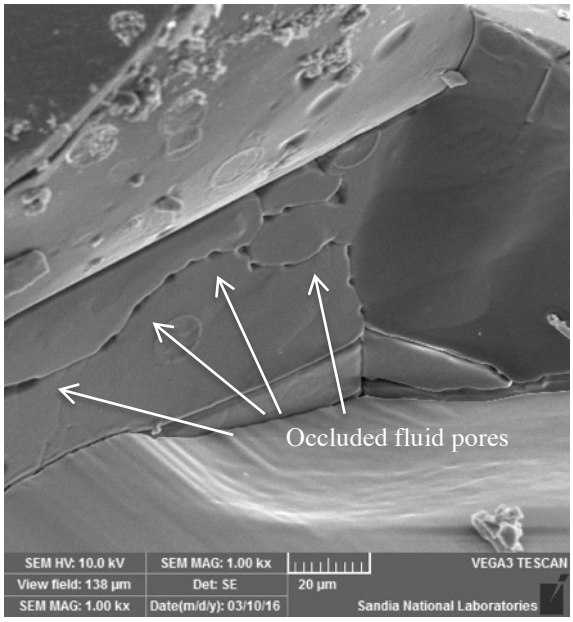

d. W90-2

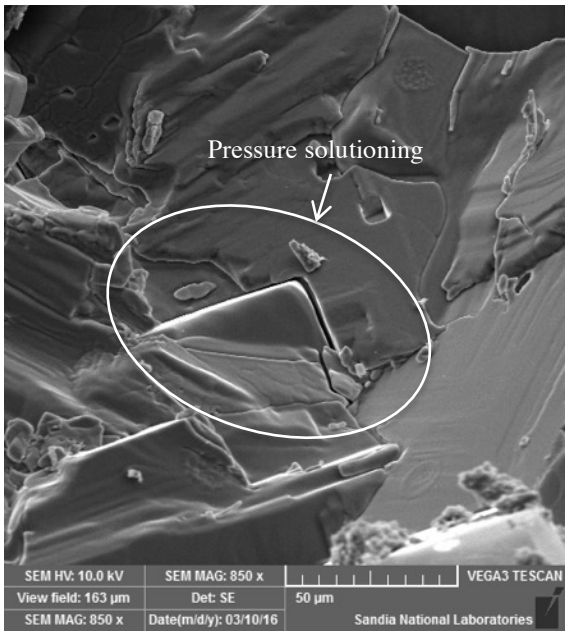

e. W90-2

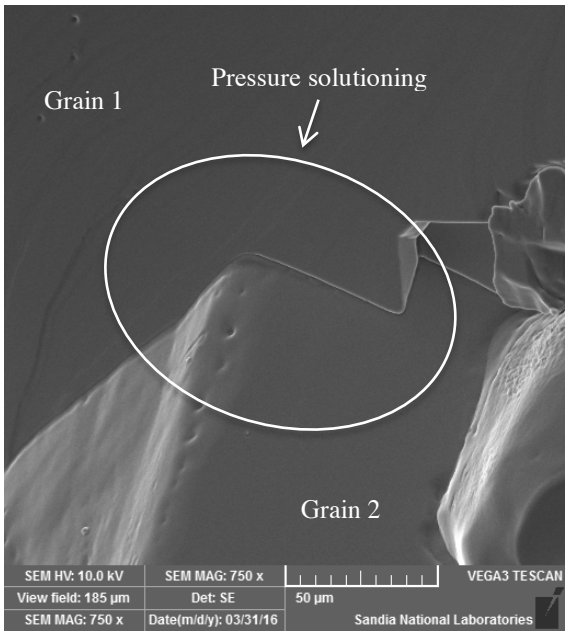

f. W90-4

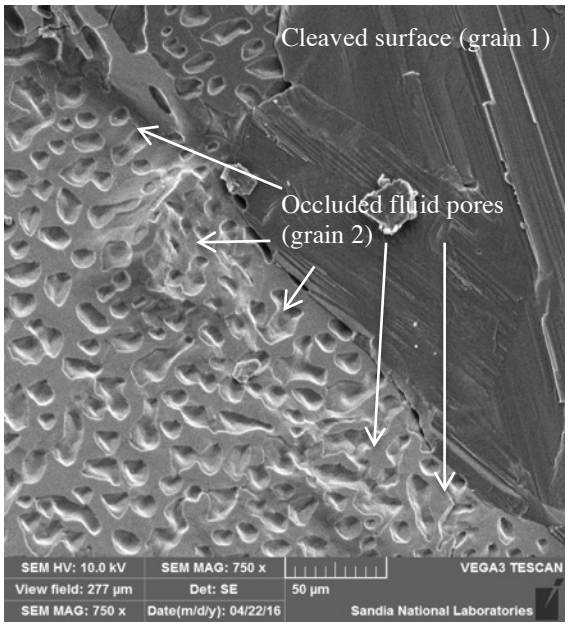

g. W90-4

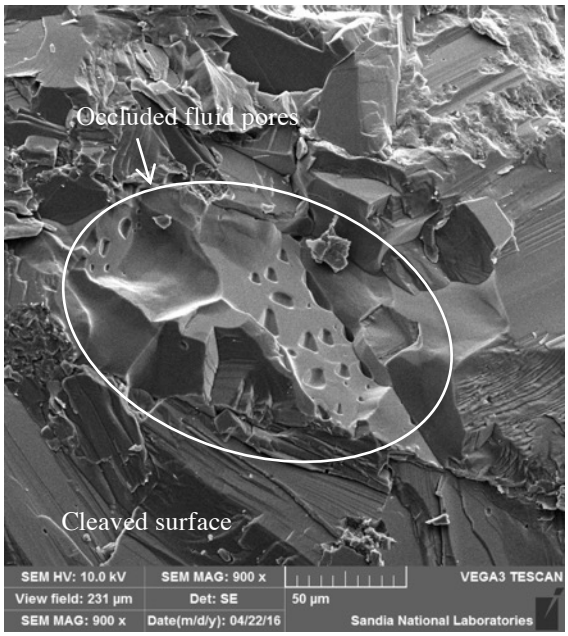

h. W90-7

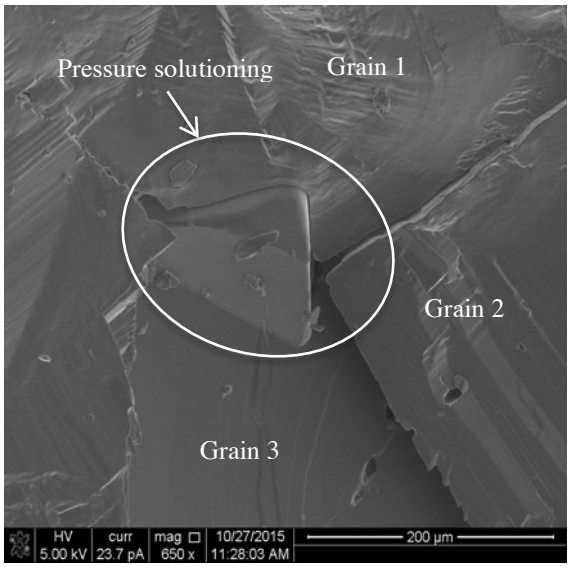

i. W90-7

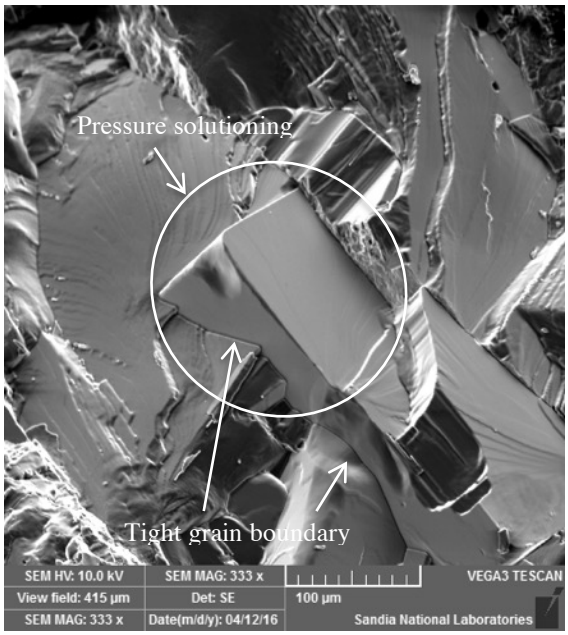

j. W90-7

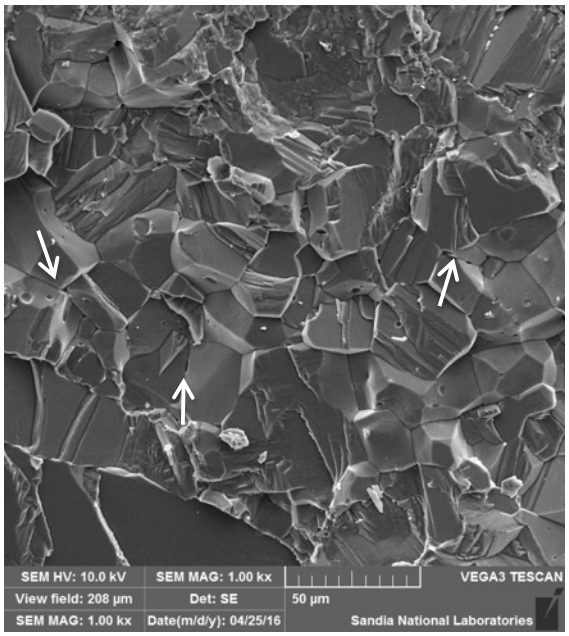

k. W90-7

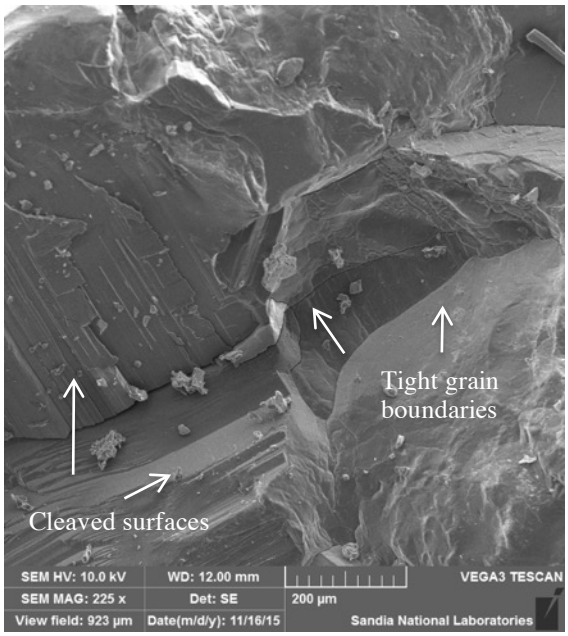

l. W250-1

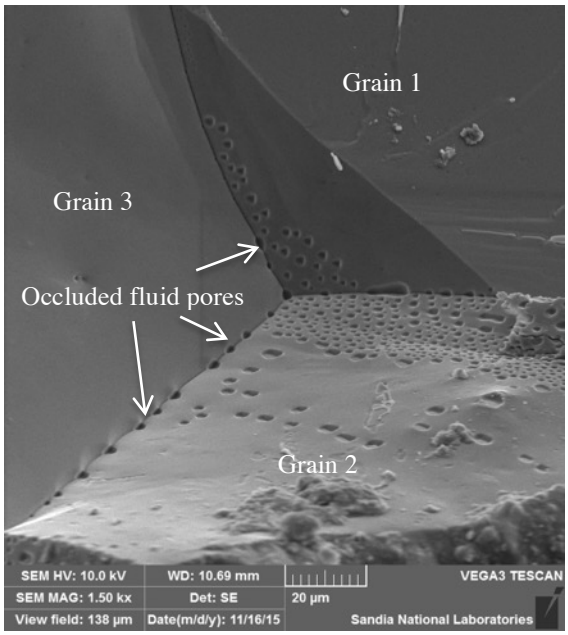

m. W250-2

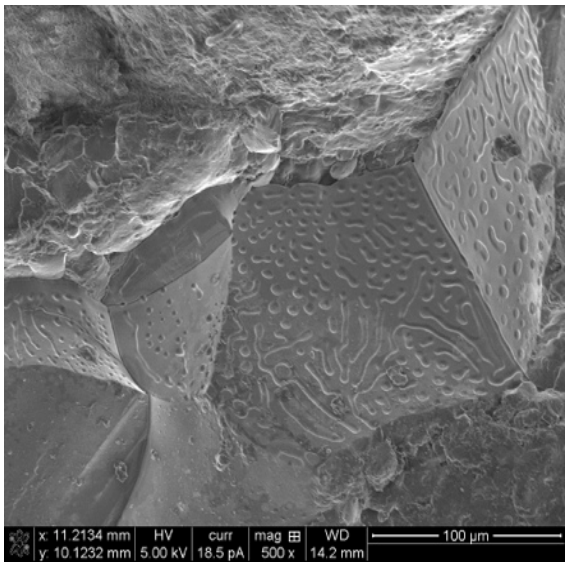

n. W250-2

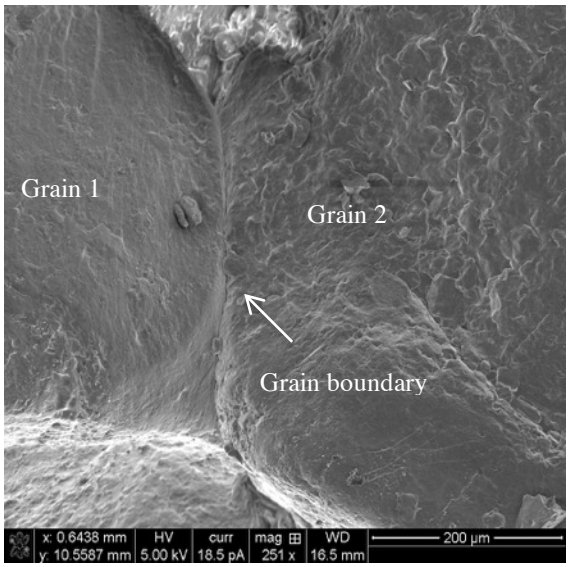

o. A250-1

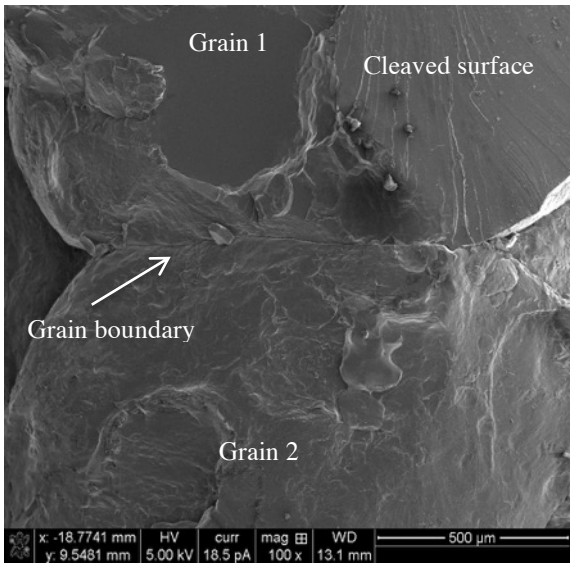

p. A250-2

Figure 3: SEM photomicrographs of mechanically broken aggregate pieces. a. W90-1: Evidence of porous spaces and mainly abraded surfaces under (500x magnification). b. W90-8: Grain boundaries with minute cohesion and rough, abraded surfaces (1,470x magnification). c. W175-1: Upper grain being plastically deformed by pressure of lower grain shown by curved 110 planes, (1,300x magnification). d. W90-2: Occluded fluid pores at center along grain boundaries and smooth, cleaved surfaces (1,000x magnification). e. W90-2: Cleaved surfaces with evidence of pressure solution by cubic grain in center protruding onto adjacent grain and tight cohered grain boundaries (800x magnification). f. W90-4: Evidence of pressure solution processes by upper deformed grain in center and traces of fluid inclusions on lower grain ridge (750x magnification). g. W90-4: Array of fluid canals and pore space imprinted on grain boundary surface (750x magnification). h. W90-7: Area of occluded fluid pore spaces at center surrounded by smoothed grain boundaries and cleaved faces (900x magnification). i. W90-7: Evidence of pressure solution in center by large grain deformation, surrounded by distorted grains from glide on <110> (650x magnification). j. W90-7: Smooth cubic grain at center with tight cohesion along grain

boundaries with traces of pressure solutioning (333x magnification). k. W90-7: Ubiquitous amount of pressure solution processes indicated by smooth cubic grains and tightly cohered grain boundaries (1,000x magnification). l. W250-1: Intersection of grains at near orthogonal orientation with tight grain boundary achieved by crystal plasticity (225x magnification). m. W250-2: Tight triple junction with canals of resided moisture displaying occluded pores (1,500x magnification). n. W250-2: Occluded fluid droplets and canals on cubic grain boundary (500x magnification). o. A250-1: Evidently tight grain boundary, but not high cohesion (251x magnification). p. A250-2: Upper grain fractured through the crystal structure while lower grain fractured on boundary and minor residual porosity (100x magnification).

Etched thin sections were imaged under a reflected and transmitted light optical microscope and are displayed in Figure 4. Figure 4a. and b. display a grain from a sample consolidated at 90°C without added moisture (W90-1). The grain exhibits a complex substructure showing bands of elongated subgrains (Figure 4a.), along with larger polygonized subgrains seen in the upper portion of Figure 4b. (denoted by X). While a similar structure is seen in the grain in Figure 4c., (W90-2 added moisture), there also appears to be areas of recrystallization evident by the highly deformed, clear subgrains in Figure 4d. This result is consistent with the presence of fluid along grain boundaries increasing grain boundary migration which lowers dislocation densities and promotes recrystallization. Although this recrystallized substructure is comparable to grains in Figure 4f., which is the unvented WIPP 250°C sample, it is not as widespread. At higher temperatures of 250°C, shown in Figure 4e.-h., samples experience much larger areas of recrystallization, with subgrain free areas (denoted by X's) surrounded by smaller subgrains throughout the crystal structure. Similar features of recrystallization on deformed Asse mine salt samples were observed in Urai et al. (1986b), consolidated at 150°C, 10 MPa, and an unknown amount of added brine.

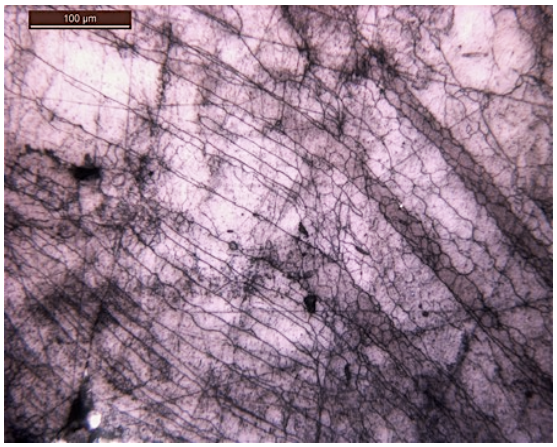

a. W90-1

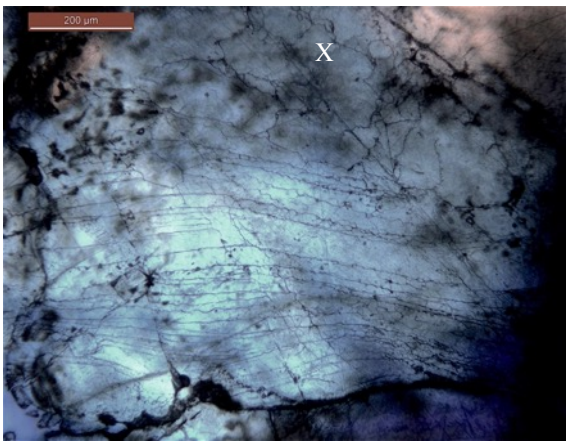

b. W90-1

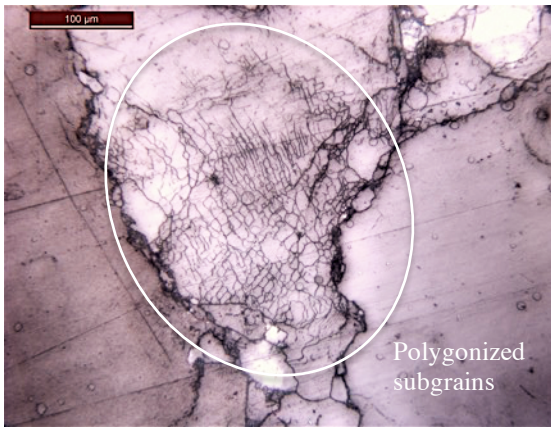

c. W90-2

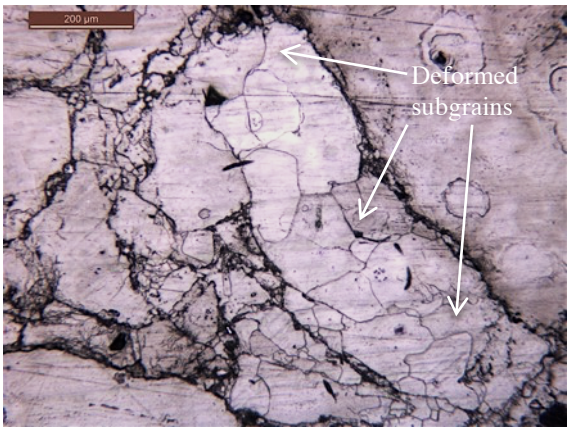

d. W90-2

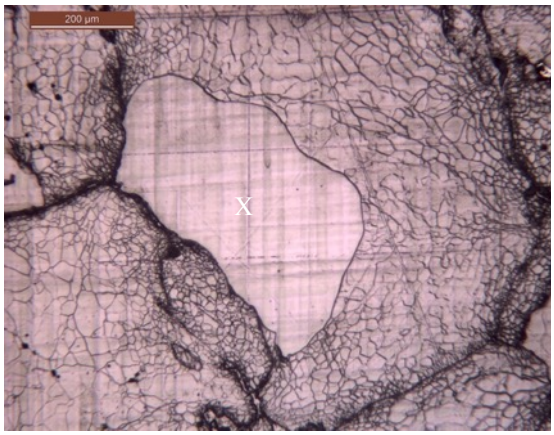

e. W250-1

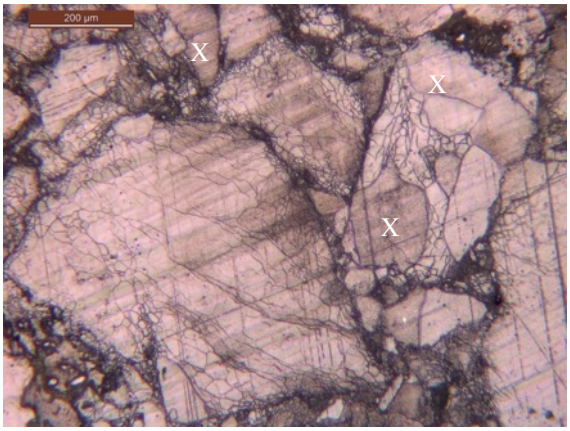

f. W250-2

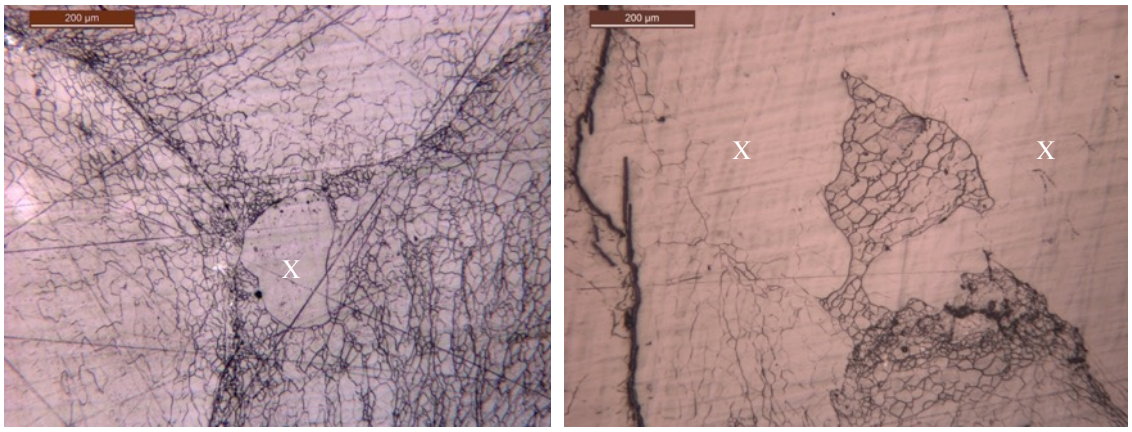

g. A250-1 h. A250-2

Figure 4. Etched thin section images under reflected and transmitted light microscope. a. W90-1: Grain with bands of elongated subgrains (20x magnification). b. W90-1: Lower magnification of grain revealing large polygonized subgrains on top of elongated subgrain bands (10x magnification). c. W90-2: Center grain with small subgrain structure with come evidence of recrystallization (20x magnification). d. W90-2: Center grain with deformed subgrain structure indicating recrystallization (10x magnification). e. W250-1: Large recrystallized area at center as well as high-energy grain boundaries (10x magnification). f. W250-2: Simultaneous recrystallization, internal grain recovery, and high energy grain boundaries (10x magnification). g. A250-1: Triple-junction grain boundary with recrystallized area in center and small subgrains decorating tight grain boundaries (10x magnification). h. A250-2: Remaining amount of subgrain structure within grain surrounded by encroaching recrystallizing area (10x magnification).

Photomicrograph results of samples with added moisture are significant because they show that a small amount of moisture added to granular salt enhances the level of fused grain boundaries and pressure solution processes, which have been primarily seen in experiments with synthetic salt. Proof of recrystallization is also significant and was somewhat unexpected since it is mainly seen in naturally deformed rock salt. Observations of recrystallization in these samples suggest that the consolidation conditions produced similar responses similar to those that occur in fully consolidated, natural salt deposits. An unexpected feature was also the occluded fluid pore spaces found in the unvented and added moisture samples.

3.2.PORE STRUCTURE RELATED PROPERTIES

3.2.1. POROSITY

Porosity measurements were obtained using four different methods and two sample types, and are displayed in Figure 5. Dimensional techniques and porosimeter testing were both made on the same sub-cored samples with a diameter of 25.4 mm and height of 12.7 mm evaluated by Paneru (2016). Dimensional techniques use an assumed salt grain density of 2.16 g/cc along with weight and volume measurements to calculate porosity. Porosimeter measurements involve helium gas expansion within a calibrated reservoir. Impregnated sample thin sections, described in Section 2, were used for point counting and image analysis. Overall, there is a general agreement between methods, and connected and total porosity are nearly the same. The image analysis method results were equal to or higher than point counting for all samples. This discrepancy could be due to the varying BSE-SEM gray scale readings from impurities (clay, anhydrite, etc.). The samples are heterogeneous, yielding a different amount of impurities and grains at each imaged location on a thin section. Thus, depending on the concentration and backscatter intensity, impurities could be included in the pore threshold, thereby increasing pore area values during image analysis calculations. In some instances, the porosimeter and dimensional technique values are higher than point counting and image analysis. One reason may be minor damages acquired from coring, which could create small cracks or expand existing pore space in samples without added water (W90-1, W90-8, and W175-1) and only preconsolidated (W90-3) because of less cohesive grain boundaries. Another reason may be due to some missed pores in the microscopic methods and/or assumptions in converting 2D to 3D measurements bias the results.

Considering specific samples at the same stress state, 90°C consolidated samples with added moisture (W90-2, W90-4, and W90-7) do experience lower porosities compared to W90-1, which had no moisture added, but a much longer test duration of 111 days. W90-3 is not included because it was only pre-consolidated, which means it was only subjected to hydrostatic stress for approximately 15 minutes. The one sample consolidated at a higher stress state of 38 MPa, W90-8, did have a lower porosity than a sample with similar conditions, W90-1, even when W90-8 had a short test duration. At 250°C, WIPP samples have similar porosities regardless of vented or unvented conditions. However, the Avery Island sample with added moisture (A250-2) yields 0.01 to 0.02 less porosity compared to a sample without added moisture (A250-1) consolidated for about the same duration.

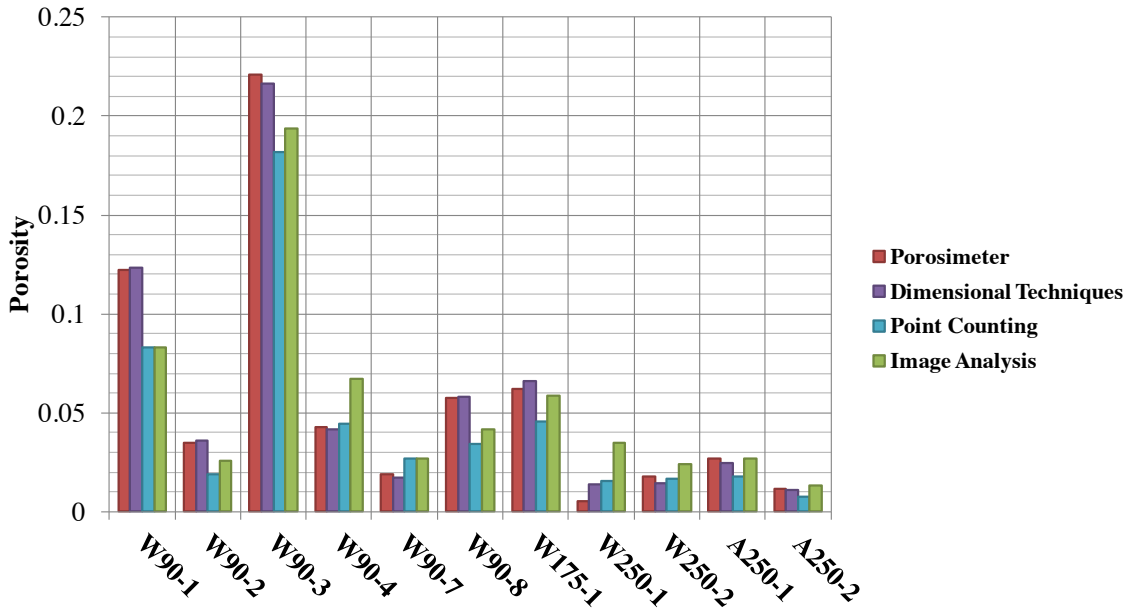

Figure 5: Comparison of sample porosity values from porosimeter, dimensional techniques, point counting, and image analysis methods.

3.2.2. SPECIFIC SURFACE AREA

Figure 6 shows specific surface area vs porosity with samples grouped by consolidation temperature. Samples with 1% moisture added are indicated in blue, while no added moisture samples are red. Specific surface area values are quite variable near or below 0.05 porosity, but there is a possible trend of increasing specific surface area as porosity decreases. This trend is expected given the relationship used to calculate specific surface area (equation 1), where samples with smaller porosities have smaller pore areas, but relatively greater perimeters and thus larger specific surface areas. Taking all samples into account, there is no clear indication that stress, temperature, and/or moisture conditions during consolidation have a direct effect on specific surface area. However, when comparing two similar samples, some influence can be seen. For instance, a higher consolidation stress (W90-8) in a shorter amount of time results in a higher specific surface area than a lower stress (W90-1) for longer periods. Also, the addition of moisture in the Avery Island sample also produces a higher specific surface area than without added moisture, while other conditions remained constant. These trends are expected because a higher stress state and addition of moisture enhances consolidation which produces a lower porosity thereby increasing specific surface area.

The box area is a range of specific surface area and porosity values obtained by Cinar et al. (2006) from experiments on compacted NaCl granulates. When compared to Cinar et al. (2006), the values of this study are larger. Cinar et al. (2006) did not use stereological relationships with petrographic image analysis, but obtained specific surface area using an areameter based on nitrogen adsorption, which could account for dissimilar values.

Other studies that used petrographic image analysis to acquire specific surface area for other types of geologic mediums include Cerepi et al (2001) and Mowers and Budd (1996). Cerepi et al (2001) analyzed carbonate limestones with variable mud to grain matrixes, where porosity ranged from 0.09 to 0.36 and specific surface area from 1400 mm^{-1} to 2500 mm^{-1}. Mowers and Budd (1996) obtained specific surface area values from 100 mm^{-1} to 500 mm^{-1} for porosities from 0.05 to 0.28 on dolomite samples. Resulting higher specific surface area values could also be indicative of included impurities in natural rock salt. The addition of moisture to samples has little apparent effect on specific surface area determinations.

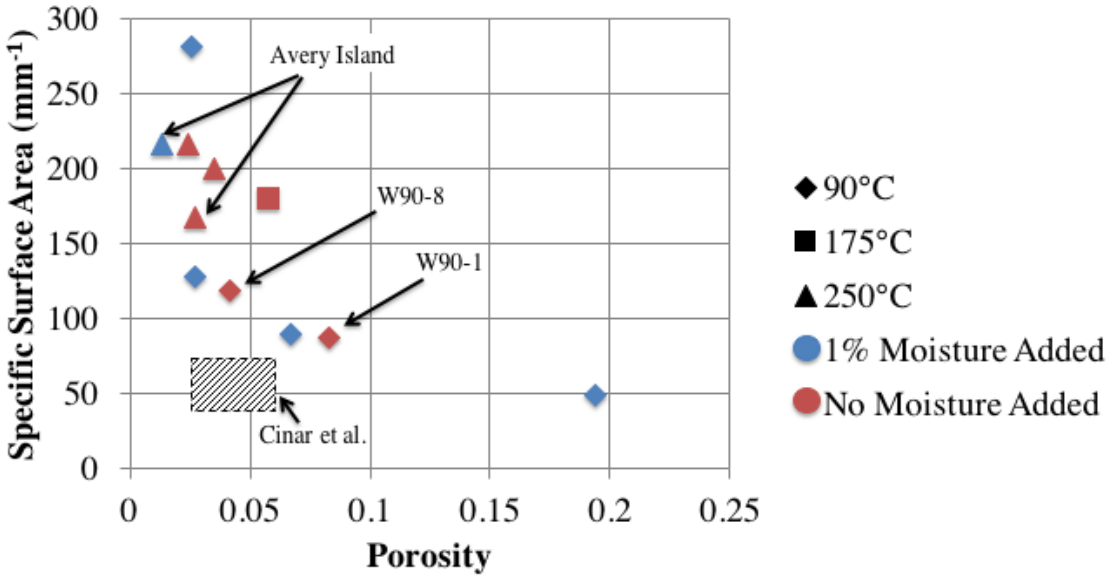

Figure 6: Comparison of specific surface area and porosity values, measured by microscopic techniques, for all samples categorized by temperature (shapes) and moisture addition (color). Range of data from Cinar et al. (2006) is also displayed.

3.2.3. PERMEABILITY

The permeabilities from four sub-cores are plotted on Figure 6 as a function of the porosity previously measured on the same sub-cores by Paneru (2016). The permeability values are corrected for gas slip. The permeabilities indicate a trend of decreasing permeability with decreasing porosity. Consistent with the concept that moisture enhances consolidation thus lowering porosity, samples with the addition of moisture (W90-4 and W90-7) experience a lower permeability than those without (W90-8 and W175-1). The difference in permeability between W90-4 and W90-7 is likely attributable to their test durations, which were 5 and 23 days, respectively. There are insufficient data to evaluate whether the permeability of a sample consolidated with additional moisture was lower than that of a sample consolidated to a comparable porosity but without additional moisture. Amongst the samples tested, permeability is shown to be impartial to consolidation conditions with respect to temperature and stress state.

Also shown in this figure are permeability-porosity relationships for granular salt based on experiments by Cinar et al. (2006) and Blanco Martin et al. (2015). The permeability of W90-8 is significantly greater than the other samples and is outside the range of displayed permeability-porosity relationships. There is concern that these small sub-cores may be damaged during coring, which could dramatically increase the permeability.

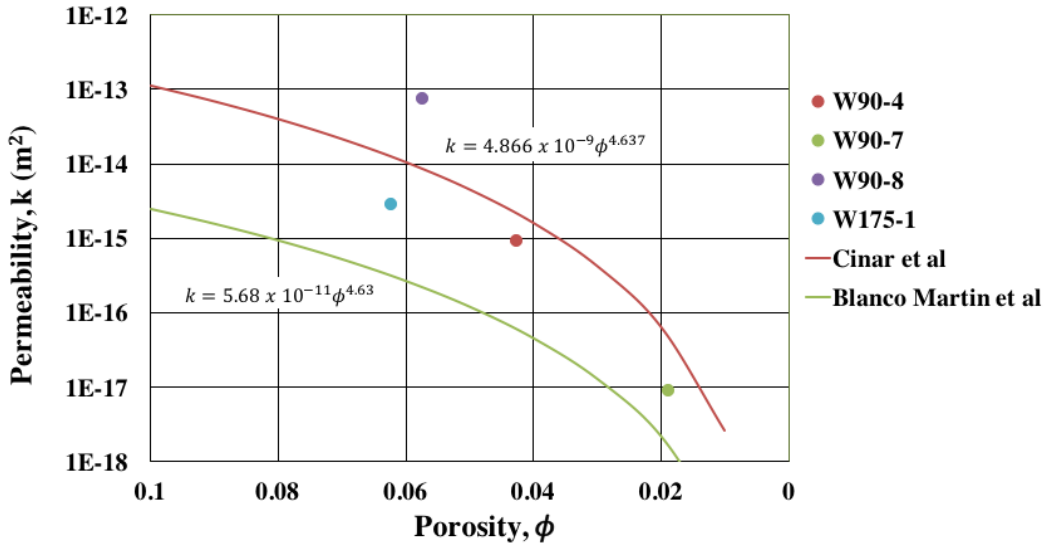

Figure 7: Permeability and porosity of selected sub-core samples, and relationship equations from Cinar et al. (2006) and Blanco Martin et al. (2015).

3.2.4. TORTUOSITY

Tortuosity is the ratio of the length of a streamline between two points in a porous medium divided by straight-line distance between the points. With this definition, tortuosity has a minimum value of one for linear flow through a porous medium. The square of this ratio is referred to as the tortuosity factor in some literature and is the term used herein.

The Carman-Kozeny permeability model was used to interpret the tortuosity factor (τ) based on permeability, porosity, and specific SA measurements made. The relationship is given by:

$$\tau = \sqrt{\frac{1}{c \cdot k \cdot SA^2} \frac{\phi^3}{(1-\phi)^2}} \qquad (3)$$

where c is the shape factor, generally taken as 2.5 (Cinar et al., 2006).

The tortuosity factor is shown versus porosity obtained from the porosimeter in Figure 8. As porosity decreases, the tortuosity factor increases which is consistent with trends observed and predicted for other porous media (e.g., Pisani, 2011). This result suggests a more convoluted pore structure in samples with added water, generating a longer traveled distance. However, the calculated tortuosity values of less than one are inconsistent with the definition of tortuosity factor. Although, it is important to note that the tortuosity is a parameter of a one-dimensional model and not a property of a porous medium (Dullien, 1991). Dullien (1991) shows how non-uniformities in the pore structure can significantly alter the interpreted permeability (or tortuosity) with the Carman-Kozeny model.

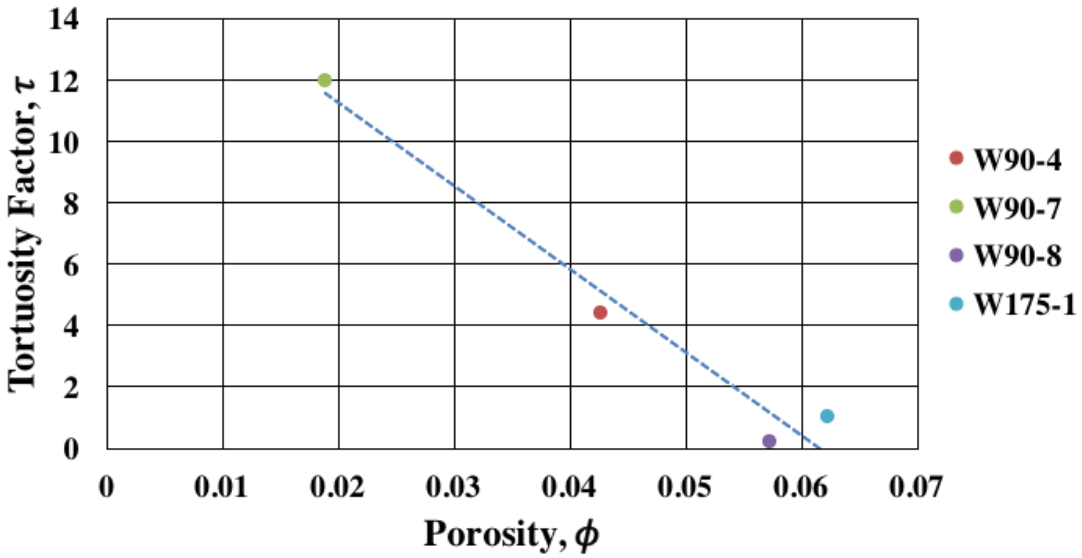

Figure 8: The tortuosity factor versus porosity for selected sub-core samples.

3.3. PORE AREA DISTRIBUTIONS

Pore areas from image analysis were separated by size due to the large range of pore areas data obtained. Pore areas were separated into two groups: micro and macro pore areas. This approach has been used by others (e.g., De Las Cuevas, 1997; Cerepi, 2001) when confronted with a very large range of pore dimensions. The measured pore areas ranged from 1.46×10^{1} to 1.96×10^{6} μm^2. Micropores were defined as less than 1000 μm^2 and macropores were defined as larger than 1000 μm^2. While this limit was somewhat arbitrary, it is similar to resolution of the human eye, which is about 40 μm in diameter, and other studies defining micropore areas to be less than 500 μm^2 (Anselmetti, 1998, Cerepi, 2001). In Figure 9, porosity versus micro-porosity is shown. The amount of porosity associated with the micropores is between 0.002 and .012, and does not appear to be a function of the total porosity. Also, the moisture condition that the samples were consolidated at does not have an apparent effect on the amount of porosity associated with micropores. The effect of the temperature upon the sample was consolidated at is not clear; four of the five samples consolidated at 90°C have a relatively low amount of micropore porosity. The 175°C thin section sample was found to contain a large amount of impurities, such as anhydrite and clays, which could explain the higher amount of micro-porosity.

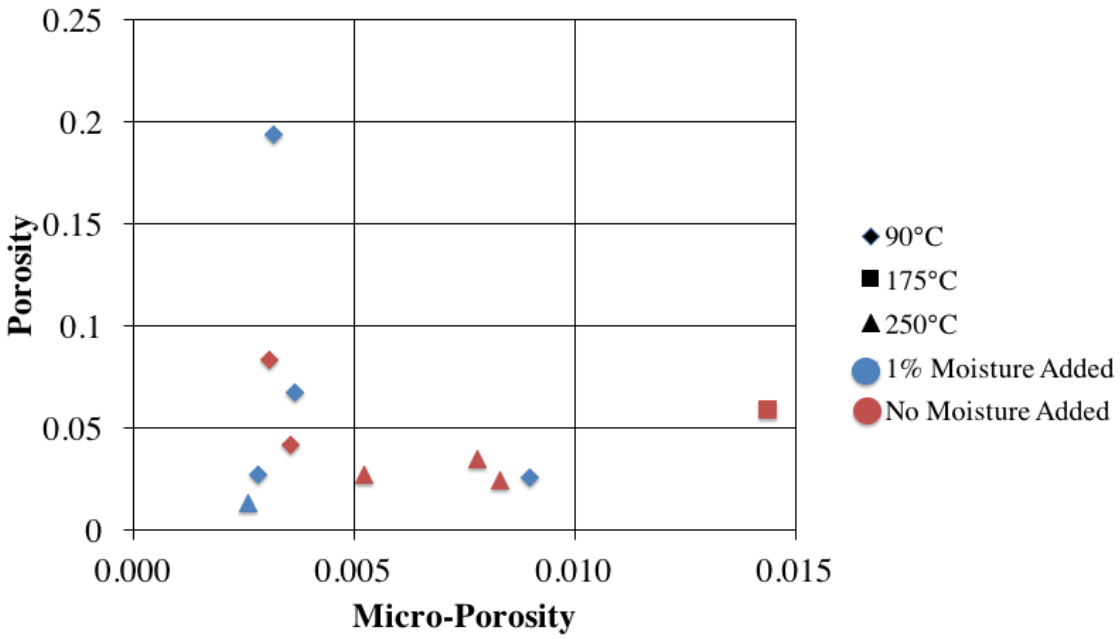

Figure 9: Total porosity versus micro-porosity with varying temperature and moisture conditions.

The following charts in Figure 10 display the distribution of micropore areas for each sample. The most frequent pore areas are the smallest bin sizes (between 15 and 75μm^2), and almost all of the pore areas are within the range from 15 to 500 μm^2 for each of the samples. Again, there is no clear indication that varying conditions have a direct influence on the range of micropore sizes. Even though stress, temperature, or added moisture do not appear to have a straightforward effect on micro-porosity, the variability of the results is interesting and unexpected. It is possible there is a stable and remnant micro-porosity when low total porosities are reached.

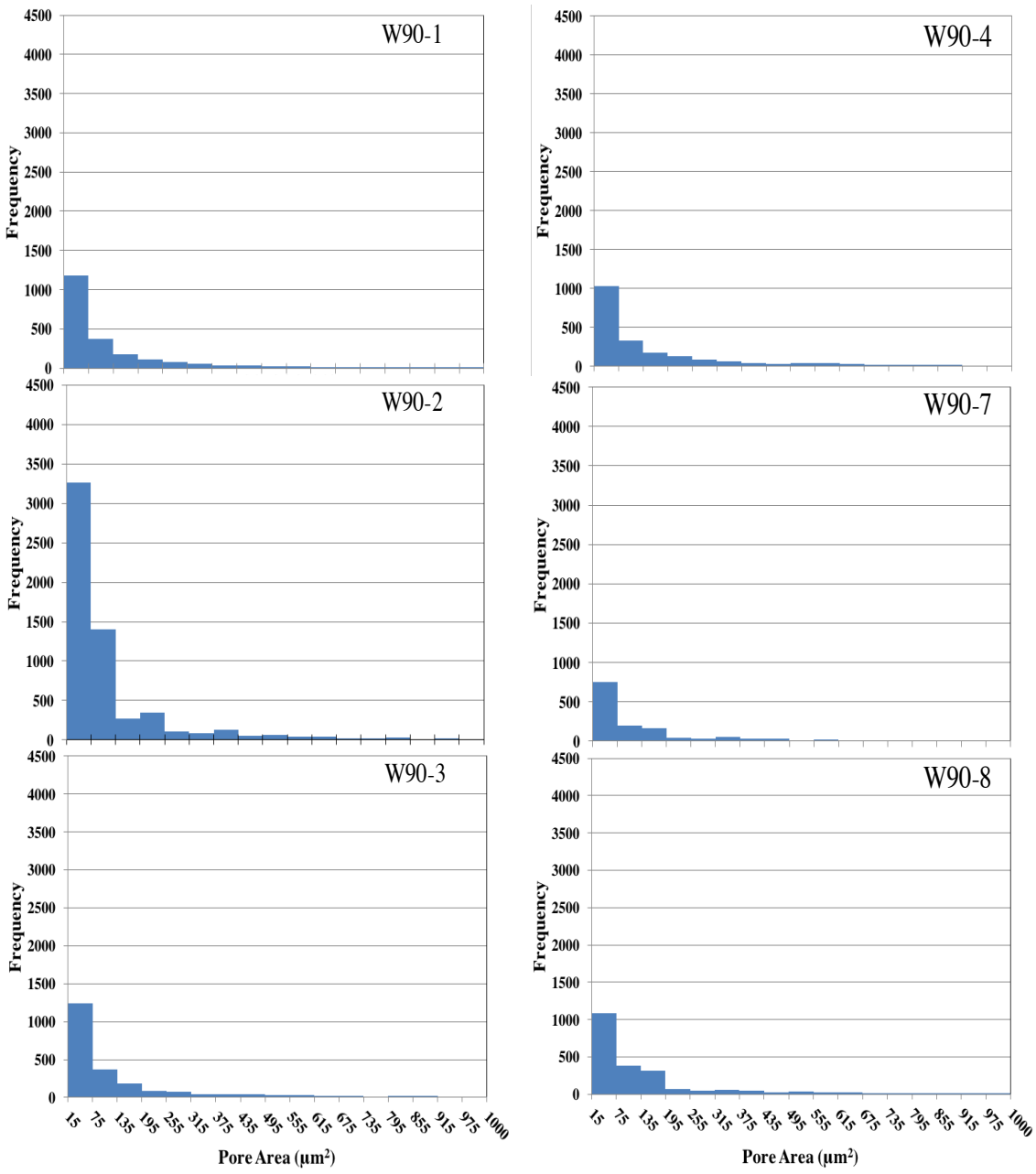
W90-1
W90-4
W90-2
W90-7
W90-3
W90-8
Frequency
Pore Area (µm²)
0
500
1000
1500
2000
2500
3000
3500
4000
4500
15
75
135
195
255
315
375
435
495
555
615
675
735
795
855
915
975
1000

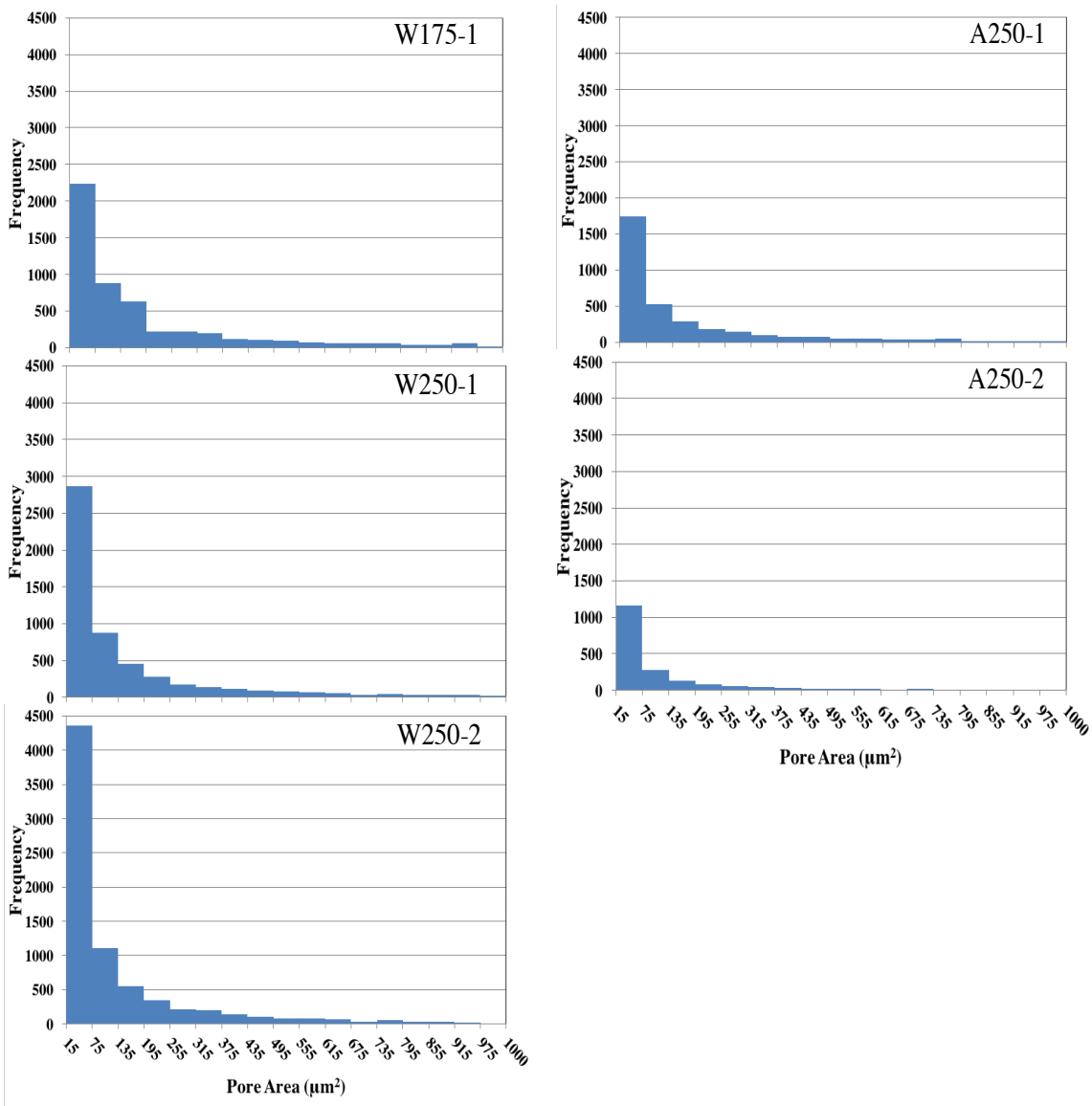

Figure 10: Micropore area distributions measured in µm^2 for each sample.

Figure 11 presents porosity versus associated macro-porosity comparison. There is a definite linear trend signifying the macro-porosity is dominant, and thus controls sample permeability. When looking at the pore area distributions (Figure 12), there is a large range of macropore areas, spanning from 1000 to 550,000 µm^2 and in some cases, even greater. In order to display all of the data, bin sizes were not equally distributed. A

majority of the macopores lie between 1000 to 10,000 μm^2. Sample W90-3 has the greatest amount of pore areas 550,000 μm^2 and above, which is consistent with its large porosity. Within the rest of the 90°C set of samples, however, there is no indication that added moisture results in fewer large pore areas. There is a slight decrease in the frequency of macropores in W250-2 as compared to W250-1, possibly due to W250-2 being an unvented sample and retaining the moisture. Comparing A250-1 and A250-2, with moisture added (A250-2), there is an apparent drop in the number of macopores. Considering consolidated samples produced at 90°C and 175°C , W90-1 had a higher frequency of large macropores (>150,000 μm^2) compared to W175-1, even when W90-1 had a much longer consolidation time. A similar result was found by Keller et al. (2014) from oedometer tests on natural crushed rock salt without water where an increase in compaction temperature led to a smaller amount of large pore sizes.

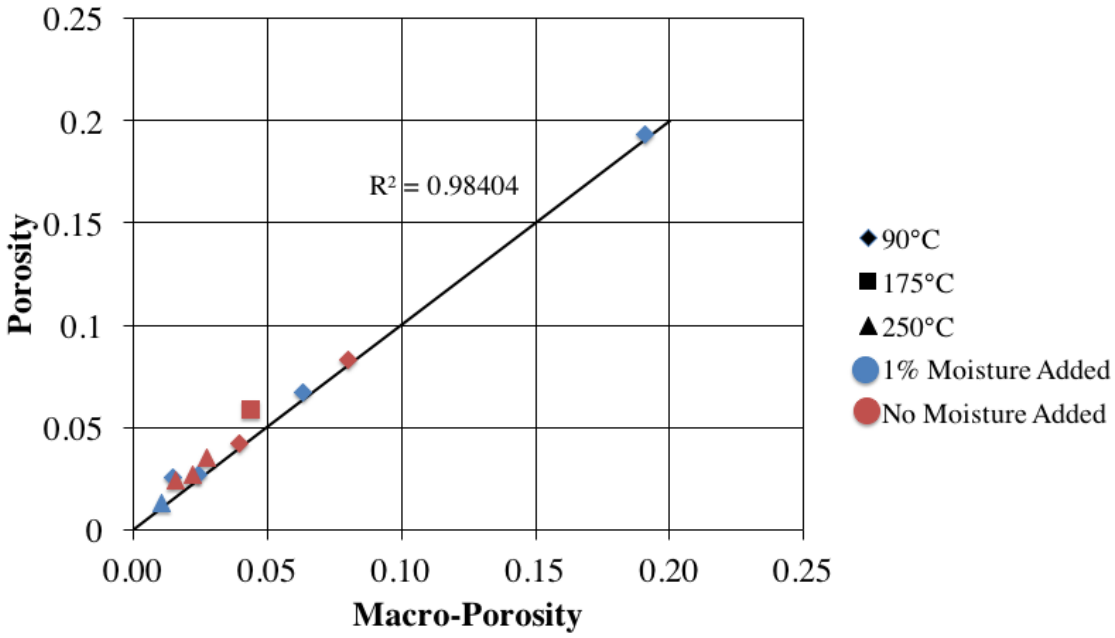

Figure 11: Total porosity versus macro-porosity with varying temperature and moisture conditions.

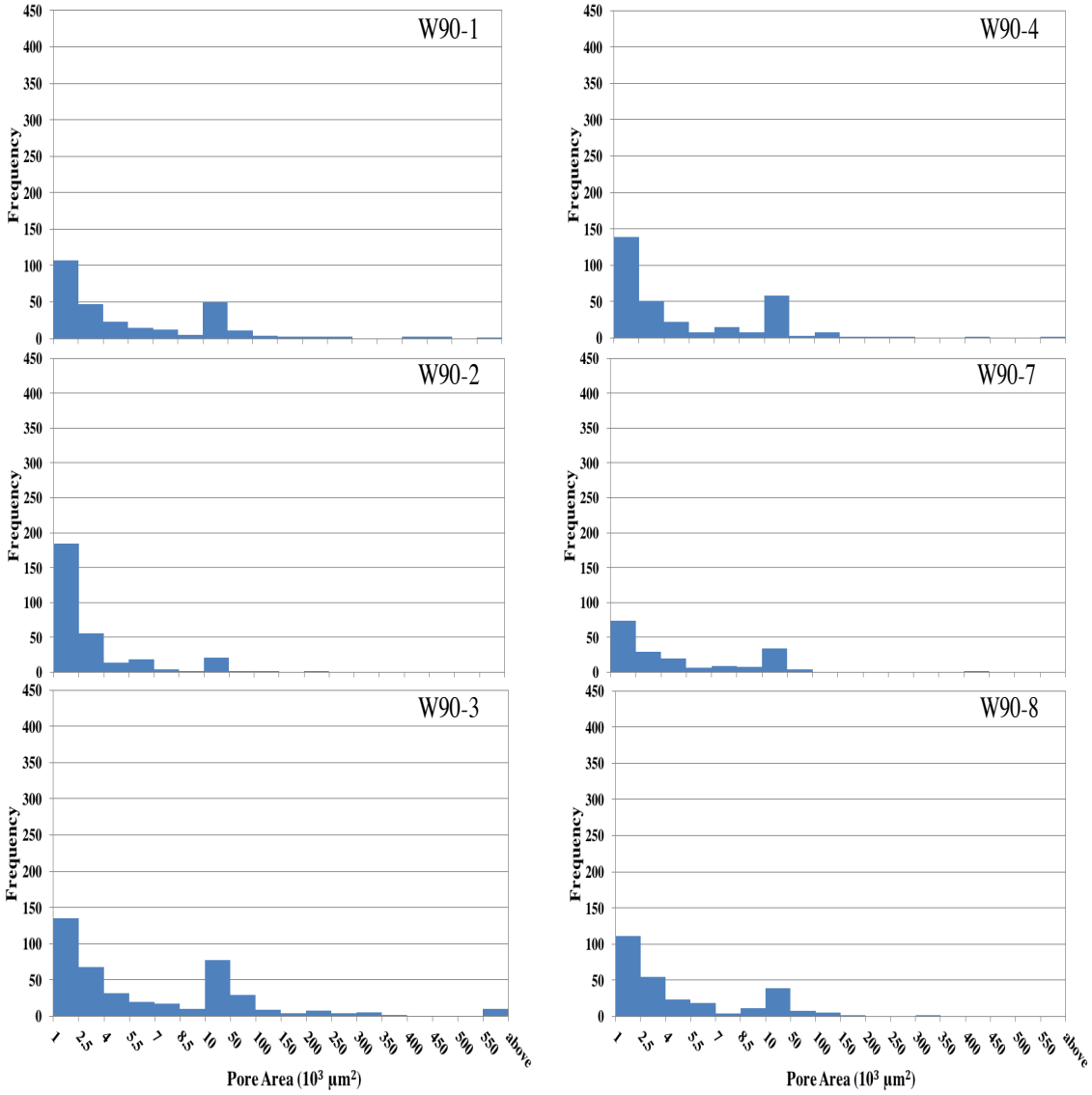
W90-1
W90-4
W90-2
W90-7
W90-3
W90-8
Frequency
Pore Area (10³ µm²)
1
2.5
4
5.5
7
8.5
10
50
100
150
200
250
300
350
400
450
500
550
above

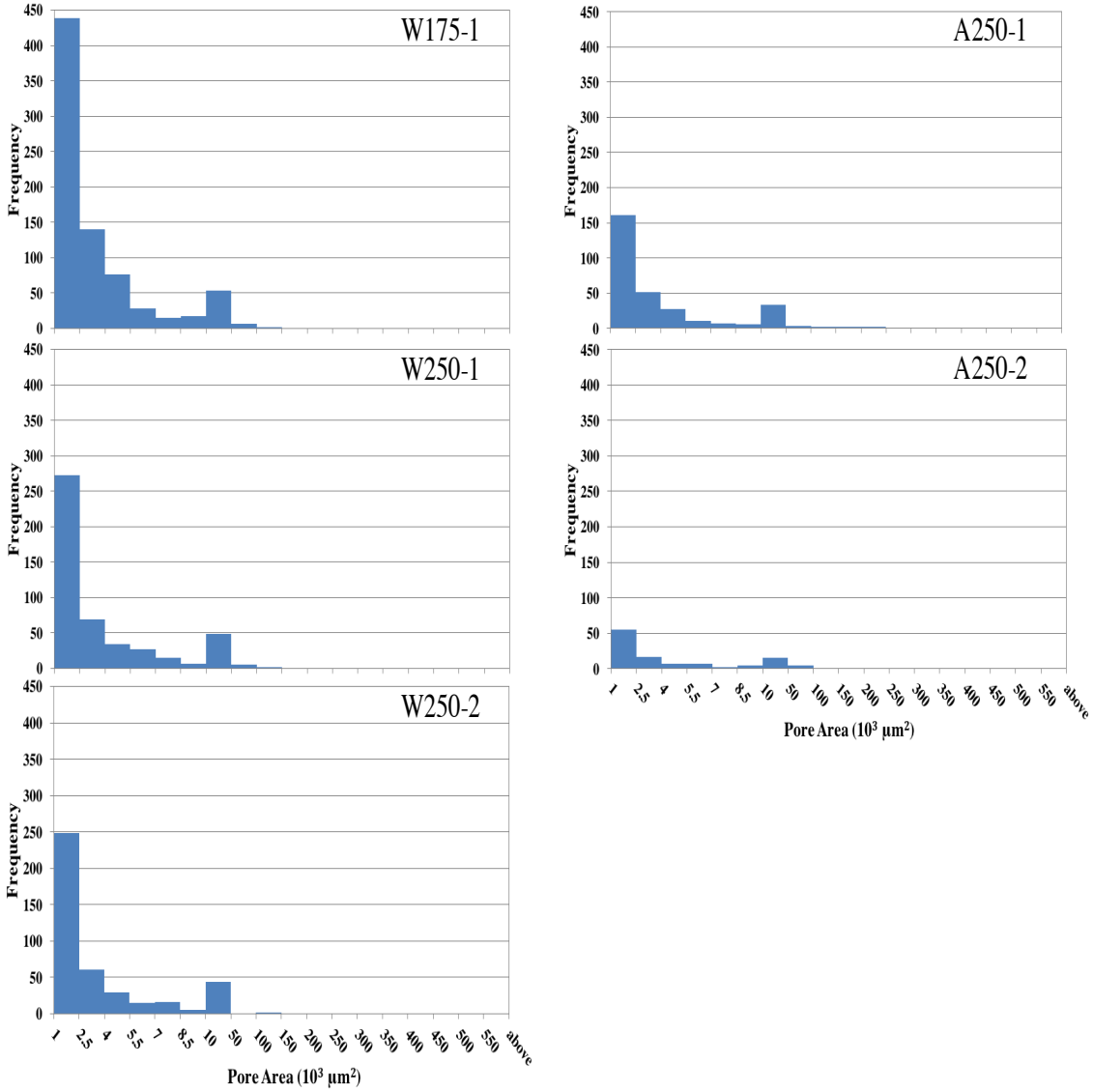

Figure 12: Macropore area distributions measured in 10^3 µm^2 for each sample.

4. CONCLUSIONS

4.1. GENERAL

Eleven laboratory consolidated granular salt samples were characterized using various methods to gather information of the operative micro-mechanics occurring during consolidation, pore properties, and pore area distributions to help understand the effects of changing stress, temperature, and moisture conditions.

Techniques for obtaining porosity values on thin sections and sub-cores relate reasonably well, and suggest that the majority of the porosity within the samples are connected even when the final porosity is less than 0.02. Discrepancies may be caused by the methods used since sub-core porosities are measurements using a porosimeter and dimensional values, while thin section methods are observational using optical and scanning electron microscopes.

A possible trend of increasing specific surface area with decreasing porosity was observed amid high variability for porosities less than 0.05. Since the PIA specific surface area relationship is based on a ratio of pore perimeter to pore area, it is reasonable that samples with large pore areas or porosity will yield a lower specific surface area.

A decrease in permeability with decreasing porosity was observed for selected samples. Permeability is dependent on pore structure and porosity, so fewer void spaces is consistent with a more limited flow path. The permeability values agree with published permeability-porosity relationships on consolidated granular rock salt.

The tortuosity factor was calculated from the Carman-Kozeny equivalent channel model using the measured permeabilities and porosities. The tortuosity factor has a trend of increasing with decreased porosity. Some tortuosity values were very near or below one which is inconsistent with the definition of tortuosity. However, the tortuosity factor is derived from a model that greatly simplifies the pore structure, and different values can be obtained by accounting for a variety of factors including pore non-uniformities. Based on the pore area analysis, samples are dominated by macropores, indicated by the linear trend of total porosity versus macro-porosity. A majority of micropore areas lied within the range of 15 to 500 μm^2, while macropores ranged from 1000 to 10,000 μm^2.

4.2. ADDED MOISTURE EFFECTS

Added moisture was found to have the biggest impact on the microstructure during consolidation. In microstructural observations, evidence of pressure solutioning was observed in samples with added moisture as well as occluded fluid pore spaces and a higher degree of cohesion found along grain boundaries. This is consistent with previous consolidation experiments noted in Urai and Spiers, 2007, showing "wet" samples deformed at stresses greater than 10-20 MPa and temperatures of 100-200°C experience fluid assisted grain boundary migration alongside dislocation creep. Documentation of occluded fluid pore spaces along grain boundaries are scarce in literature, but have been seen in Urai et al., 1986b, on deformed Asse mine samples. Samples consolidated at 90°C (W90-1 and W90-8) and 175°C (W175-1) without added moisture show no

evidence of pressure solution processes, only plastic deformation. Recrystallization was also seen in etched thin sections at 90°C with added moisture.

Comparing porosities of 90°C consolidated samples, those with added moisture (W90-2, W90-4, and W90-7) do experience lower porosities than those without added moisture (W90-1 and W90-8); W90-3 is an exception due to only being preconsolidated. At 250°C, WIPP samples have similar porosities regardless of vented or unvented conditions. However, the Avery Island sample with added moisture does have about a 0.01 to 0.02 drop in porosity compared to no added moisture at similar conditions. Overall, the addition of moisture had no effect on specific surface area of WIPP samples, but within Avery Island, the sample with added moisture produced a higher specific surface area. From the samples tested with the permeameter, samples with added moisture, W90-4 and W90-7, had lower permeabilities and tortuosity factors, where W90-7 experienced even lower values that W90-4 due to a longer test duration. There was little effect on micro-porosity with different consolidation conditions, but there appeared to be a lower frequency of macropores in 250°C samples that retained or had added moisture compared to other similar samples.

4.3. TEMPERATURE EFFECTS

The 250°C samples did have a higher degree of cohesion along grain boundaries and lower porosities overall. Comparing W90-1, W175-1, and W250-1, which had the same stress and moisture conditions, the higher temperature samples experienced a lower porosity, higher specific surface area, higher micro-porosity and frequency of

micropores, even though W90-1 was subject to a much longer consolidation time. Recrystallization was also observed prominently throughout sample grains of both WIPP and Avery Island salt consolidated at 250°C. When looking at the WIPP samples, the higher consolidation temperatures show a larger frequency in the lower end of the macropore range from 1000 to 2500 μm^2.

4.4. STRESS EFFECTS

The one sample consolidated at a higher stress state was W90-8 at 38 MPa, which was directly compared to W90-1. Considering both at the same temperature and moisture conditions, W90-1 had a long test duration, yet a higher stress state in W90-8 resulted in a lower porosity. W90-8 also had a higher specific surface area and a lower frequency of large macropores. There were no apparent differences in sample morphology within the microstructural observations or in micro and macro-porosity. Not enough information was gathered to determine the impact of stress on permeability and tortuosity.

APPEDICES

APPENDIX A: EQUIPMENT AND EXPERIMENTAL METHODS

APPENDIX B: FLUID INCLUSION TRANSFORMATION IN NATIVE SALT CLEAVAGE CHIPS

APPENDIX C: OBSERVATIONAL STUDIES FROM BAMBUS II EXPERIMENT

APPENDIX D: OBSERVATIONAL STUDIES FROM PREVIOUS SANDIA NATIONAL LABS GRANULAR SALT CONSOLIDATION EXPERIMENTS

APPENDIX A: EQUIPMENT AND EXPERIMENTAL METHODS

A.1. EQUIPMENT

The JEOL 5800LV scanning electron microscope, Figure A-1, uses a beam of electrons to scan a sample in order to create images of the surface at high magnification up to 300,000x. It can also be used to determine the composition of a sample based off the signals produced by atoms within the sample and the electrons. The JEOL is equipped with secondary and backscattered electron imaging detectors as well as a cathodoluminscence (CL) imaging detector. It is a low pressure microscope that operates at high and low vacuum. The instrument uses the Oxford Isis 300 analytical system, which includes an energy dispersive spectroscopy (EDS) detector, to acquire sample images and composition.

Figure A-1: JEOL 5800LV scanning electron microscope.

A FEI Nova 200 Nanolab, Figure A-2, is an instrument with a dual beam system of a focused ion beam column and SEM column. The SEM column is equipped with a tungsten filament for imaging in low or high vacuum levels. The detector has a resolution of 3.5 nm operating at 30 kV at high vacuum and less than 15 nm at 3 kV when operating in low vacuum. The instrument is also equipped with INCA Synergy 350 with HKL Premium EBSD System, which allows elemental analysis of samples as well as the capability of generating phase maps from elemental maps and Cameo data. Samples up to 12 inches in diameter can then be mapped. A HKL Premium Electron Backscatter Detector can be used within the machine for crystallographic determination to create orientation maps of microstructures, generate combined orientation and elemental maps, and generate pole figures.

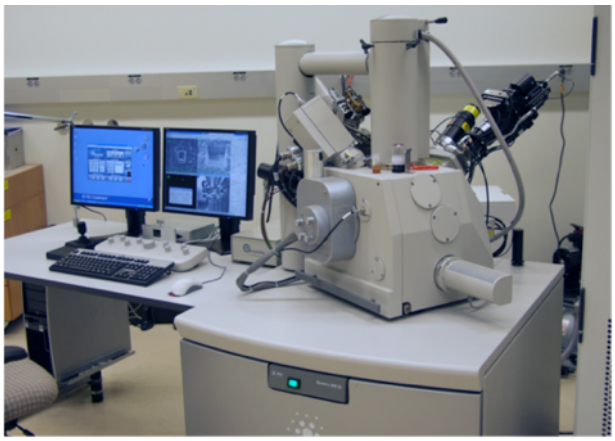

Figure A-2: FEI Nova 200 Nanolab SEM.

The Tescan Vega3 LM SEM (Figure A-3) is equipped with a conventional tungsten heated cathode that can be used in high vacuum or low vacuum. Resolution down to at least 3 nm, an accelerating voltage range from 0.2 to 30 kV, and continuous magnification from 2.5x to 1,000,000x produces excellent images for observational work. The large analytical chamber with a 5-axis motorized stage permits easy placement of multiply sample types. The EDX and EBSD enabled ports allow for elemental analysis spectrums and back scattering detection.

Figure A-3: Tescan Vega3 LM SEM.

In order to prepare non-conducting or poorly conducting samples for observation in a SEM instrument, a sputter coater must be used. The EmiTech KX950 sputter coater, Figure A-4, allows for samples to be thinly coated by carbon or gold-palladium to increase the electrical conduction. The palladium acts as a physical barrier to the gold, which attempts to conglomerate into large islands and restrict ultimate resolution performance. It is equipped with a turbo pump evaporator for complete automatic control during evaporation of the chamber to low pressures while having a dry gas inlet to improve deposition of the coating. This sputter coater is also used with a K150X film thickness monitor that measures the thickness of the coating that has been deposited on a

crystal within the chamber. It allows for accurate measurements in case some samples have more delicate features than others, such as an etch, and too thick of a film will diminish these features.

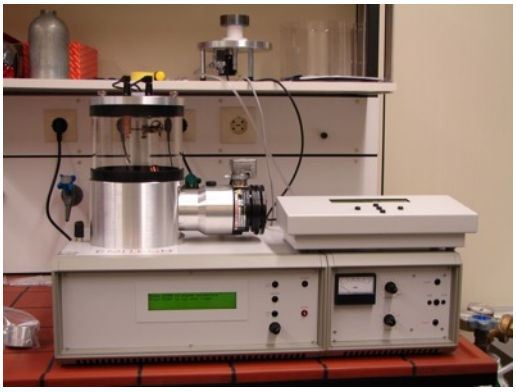

Figure A-4: EmiTech KX950 sputter coater with K150X film thickness monitor.

Using the sputter coater, samples could be coated in carbon or gold-palladium to view within the SEM. A carbon rod with a 3mm sharpened spigot shaped head is ignited and evaporated producing a 25nm thick coat for a 5 second pulse. Carbon coating is generally used for the unetched, consolidated mass samples since greater detail is not as desirable. However, for samples that have been etched, gold-palladium is used to produce high-resolution coating. A consistent problem when coating has been figuring out the most favorable thickness. Too thick of a coating will cover the subgrain features produced by the etch, while too thin will not highlight them enough to be observable. From a series of tests with samples each coated different thicknesses, 9.5nm produced the best results to view the etched subgrain features.

A Leitz Ortholux II optical microscope, Figure A-5, uses combined transmitted and incident polarized light with a five objective nosepiece to examine samples. The microscope is equipped with a Leica camera and Lieca Application Suite software to capture images of any sample.

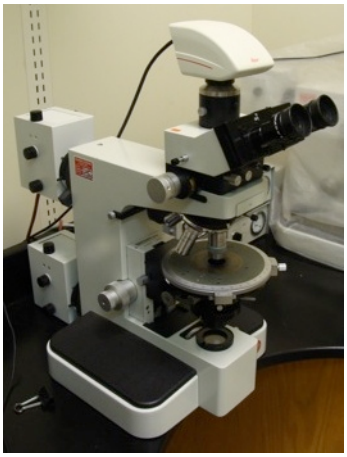

Figure A-5: Leitz Ortholux II optical microscope.

After salt is consolidated into lead jacketed cylinders, the samples needed to be cut in order to make thin-sections, obtain aggregated samples, and perform thermal conductivity tests. A diamond wire saw, shown in Figure A-6, is the best type of saw to cut rock salt due to its semi-fragile nature. The sample is first placed on the platform, making sure it is stable by using weights or clamps, so it does not move while cutting. The wire arm is then lowered just above the sample and then the pump is turned on for the rotating wheel. The wheel changes rotating directions due to magnetic sensors, which allows the wire to be pulled back and forth. By placing a small amount of weight of about 5 grams on the wire arm, the arm lowers slowly down through the sample. Sensors located on the sides of the arm control how low the wire goes and effectively shuts off the pump once the arm is close.

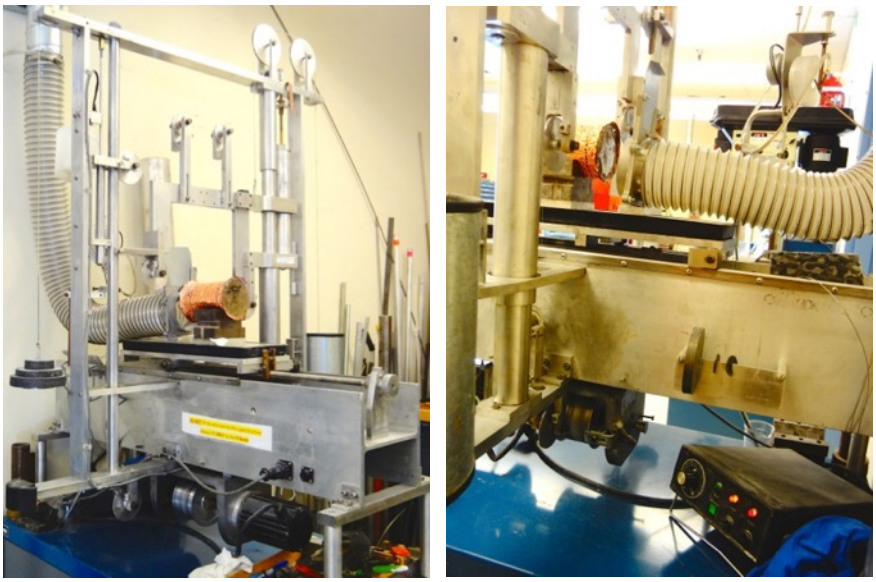

Figure A-6: Diamond wire saw with ventilation, pulley system, adjustable table, wheel, pump and pump controller.

A Buehler IsoMet low speed saw, shown in Figure A-7, is used for making precision cut thin sections with a diamond tipped saw. Once the surface of an impregnated sample is glued to a glass slide, the slide is suctioned into a vacuum chuck holder with the help of a small amount of vacuum grease to create a tight seal. The holder is then screwed onto the arm above the blade and its position adjusted by a micrometer. The micrometer allows for manual determination of thickness for each cut. Weights on the arm control the loading of the specimen, which governs the speed of the cut. For salt specimens, isopropanol is used as the cutting liquid and is poured into a reservoir below the blade, refilling regularly due to evaporation.

Figure A-7: Buehler IsoMet low speed saw.

Figure A-8 shows a Buehler Ecomet III polisher and grinder, which is used to polish thin sections after cutting and also to create smooth, even surfaces for porosity samples. Abrasive, circular paper, ranging in grit size from 400 to 1200, is adhered to a rotating wheel. The paper is wetted with isopropanol and samples are held on the wheel with minimal pressure until a smooth surface is acquired.

Figure A-8: Buehler Ecomet III polisher and grinder**.**

A.2. SAMPLE PREPARATION

A.2.1 IMPREGNATION AND THIN SECTION SLICING

Typically, the solid state of the sample is locked in place by impregnation with low viscosity epoxy. Samples are shaped to a convenient size for thin- or thick-section preparation using the slow-speed, low damage diamond wire saw. There are many types of epoxy that can be used. Two low viscosity epoxies were chosen and used for impregnation. A two-component epoxy, stained blue, was used in commercially manufactured thin sections (RF 1366 commercially available epoxy from Resin Formulators). The Spurr Low-Viscosity Embedding Kit, available from Sigma-Aldrich®,

was also used and doped with rhodamine dye for color contrast. The sub-sample is placed in a convenient disposable container (a paper cup, plastic bag, or aluminum foil, for example). The sample is completely immersed in epoxy and placed in a bell jar, which is put under vacuum and pressurized until epoxy just starts to boil. After the system has been evacuated, the vacuum is removed slowly by venting and atmospheric pressure helps force epoxy into the evacuated voids of the specimen. This process is repeated 3-4 times to ensure that the specimen has been fully impregnated. The epoxy is then allowed to cure. Spurr epoxy required to be cured in an oven at 50°C to 70°C. After curing, excess epoxy is removed and the side for thin sectioning is grinded down with the lap plate to create a smooth, flat surface. After smoothing, a glass slide is glued on with 5-minute Devcon epoxy. The Isomet saw and sample holders described in the equipment section is then used to accurately cut thin sections. Mineral oil and isopropanol were used as the cutting fluid.

A.2.2 POLISHING

To improve imaging on the stereo-dynascopic or optical microscopes, uneven surfaces after cutting need to be smoothed by polishing. This is done using a clean, flat surface with a sheet of sandpaper and isopropanol, or the Buehler lap plate with circular adhesive grit. For salt, silicon carbide grit sizes ranging from 120 to 1200 provided efficient material removal and polishing. For thin sections specifically, a series of higher grit sizes (400, 600, 800, and 1200) was used for optical microscopic observations in reflected light. Isopropanol is used as the wetting agent and a figure-eight motion creates a nice, even finish.

A.3. EXPERIMENTAL METHODS

A.3.1. CLEAVING AND ETCHING

Etching is a technique that allows for heavily deformed grains under multiple mechanisms to be highlighted. Individual cleavage chips are etched to highlight the substructure in the crystal lattice. Pits etch preferentially because atoms around dislocations possess strain energy and are more readily taken into solution by the etchant. Cleaving a sample involves using a small hammer and chisel on a single salt grain along the Miller Indices {100} plane. This produces a roughly planar, flat surfaced chip that is about 0.1-0.2 cm thick and can then be etched. A solution of methanol saturated with $PbCl_2$ is used as the etchant and stopped with butanol. Etching requires practice. Typically, the single chip is held with a tweezers and agitated in the $PbCl_2$ solution for 3 to 4 seconds and stopped immediately by transfer to butanol. Excess liquid can be drawn off by dropping the chip on a dry Kimwipe®. Immediate examination on an optical scope allows evaluation of how well etching was done. Crisp etches with sharp contrast and resolution allow for better evaluation of the substructure. After cleavage chips are successfully etched, they are mounted with carbon tape and coated in gold-palladium for observation under the SEM where a higher magnification and resolution of the etched surface can be seen.

A.3.2. POINT COUNTING

A thick-thin or thin section is placed on a mechanical slide stage, shown in Figure A-9, on an optical microscope. This slide stage moves in the horizontal direction 40 mm and 20 mm in the vertical direction, where one rotation between nob notches is equal to 1mm. The sample is moved within the stage in a grid-like pattern with an equal distance in the vertical and horizontal directions. As the sample is moved, it is determined whether the eyepiece crosshairs are located on void space or solid space. This is what is known as a count. Typically, about 300 to 500 counts must be made per run to obtain a more accurate measurement. The direction of movement must also me changed after each run in order to get a better representation of the entire sample.

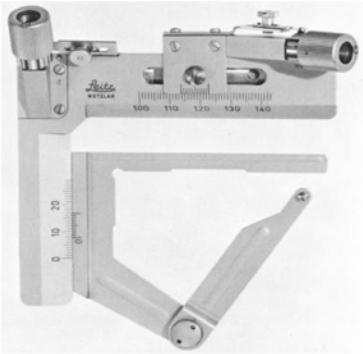

Figure A-9: Leitz mechanical slide stage for optical microscope.

APPENDIX B: FLUID INCLUSION TRANSFORMATION IN NATIVE SALT CLEAVAGE CHIPS

B.1. PURPOSE

The purpose of this experiment was to perform incremental heating on cleavage chips for two types of natural salt, WIPP (bedded) and Avery Island (domal). Observations made on an optical microscope in reflected and transmitted light were implemented to document changes in fluid inclusions at heating increments. Any mass loss associated with heating was also recorded after various heating periods, which relates to the evaporation of any free fluids.

B.2. EXPERIMENTAL PROCEDURE

Two cleavage chips from native mine-run WIPP salt and two from Avery Island salt grains were produced for this experiment by means of a chisel and hammer. One of the WIPP samples was cleaved from a highly mineralized grain in order to see the effects associated with impurities. The other WIPP sample was from a very pure grain. All samples were looked at under an optical microscope prior to heating in order to find interesting fluid inclusion locations and acquire baseline photomicrographs. Prevalent fluid inclusion areas were of specific interest in this study. These areas were mapped so they could be located after each temperature increment to associate any changes that occurred after heating and cooling.

The tare weight of four aluminum weigh boats was obtained and were used to hold each sample during heating. The total weight of the cleaved sample and weigh boat was also recorded, so the individual cleavage chip weight could be found. Using a forced air convective oven, samples were heated beginning at 100°C for at least 20 hours. The temperature was increased by increments of 50°C up to 250°C. Microscopic observations were made at the designated areas of interest along with sample weigh measurements after every incremental heating period. They were allowed to cool for approximately 5 minutes prior to weighing to ensure air currents associated with temperature differences did not distort mass results. After the maximum temperature of 250°C was reached, a reverse heating procedure was done by lowering the temperature in 50°C increments, again holding for at least 20 hours. This was done in order to see if any affects observed were permanent or reversible. Lastly, the samples were allowed to cool at ambient temperature for three days until final photomicrographs and weights were acquired.

B.3. EQUIPMENT USED

- Small hammer
- Small chisel
- Aluminum weigh boats
- Tweezers
- Scale

- Mettler Toledo XS205 Dual Range balance with readability measurements to 0.1 mg to identify small amounts of weight changes.

- Oven
  - A medium sized, 120V Fisher Scientific Isotemp Premium Lab Oven with forced convective air and range of 50°C to 275°C in increments of 1°C.
- Microscope
  - A Leitz Ortholux II optical microscope that uses combined transmitted and incident polarized light with a five objective nosepiece to examine samples. The microscope is also equipped with a Leica camera and Lieca Application Suite software to capture sample images.

B.4. RESULTS

B.4.1. WEIGHT CHANGE

As the samples were incrementally heated, weights were recorded in order to determine the total percent weight change after the experiment was completed. The graphs below in Figures B-1 to B-4 provide the results for the weight change for each of the samples as the temperature was raised and then lowered.

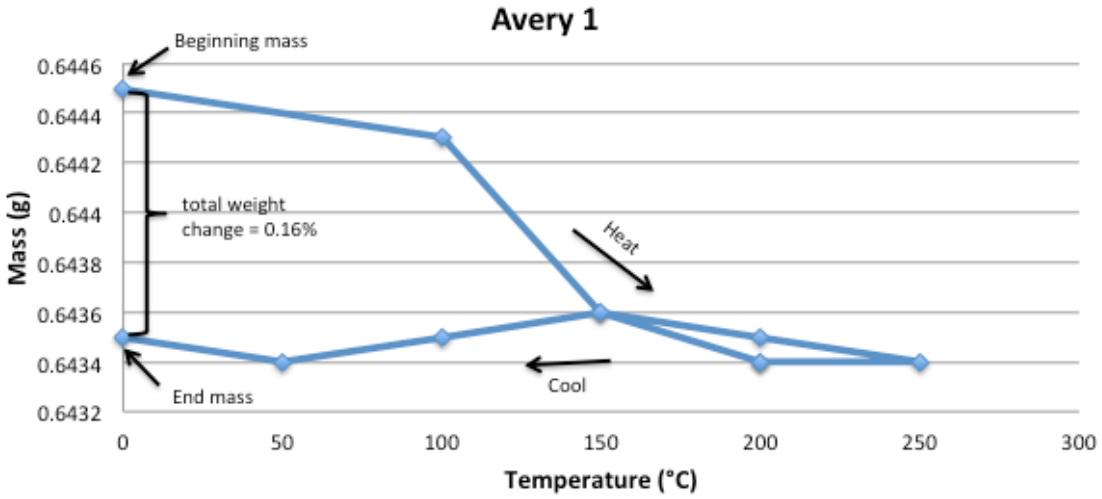

Figure B-1: Mass as a function of temperature for Avery Island sample 1 showing total weight loss.

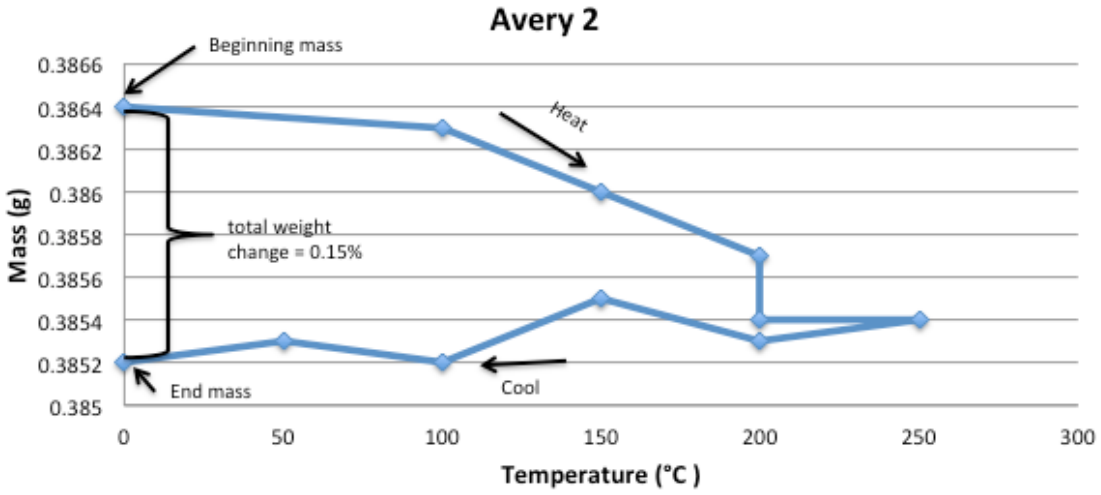

Figure B-2: Mass as a function of temperature for Avery Island sample 2 showing total weight loss.

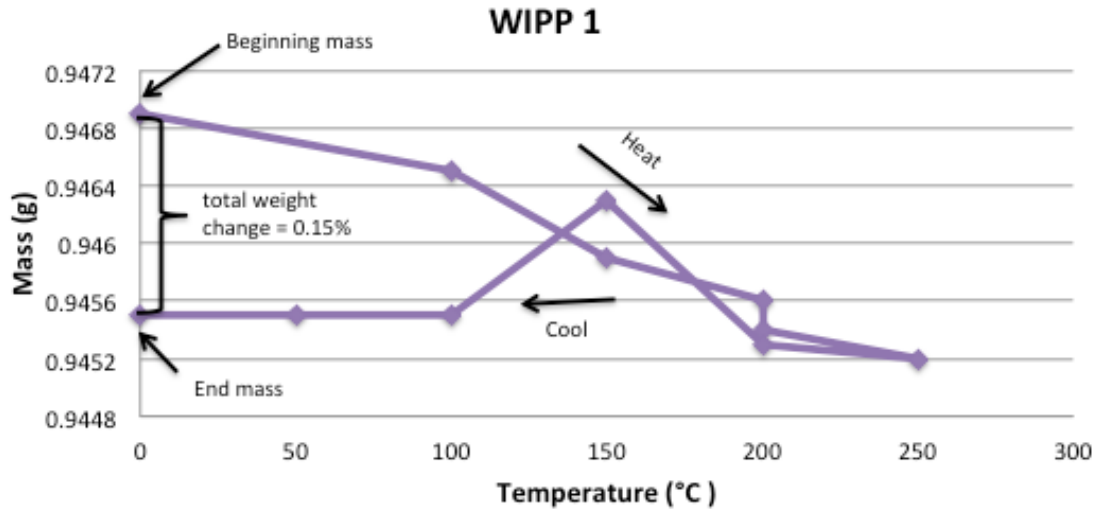

Figure B-3: Mass as a function of temperature for WIPP sample 1 showing total weight loss.

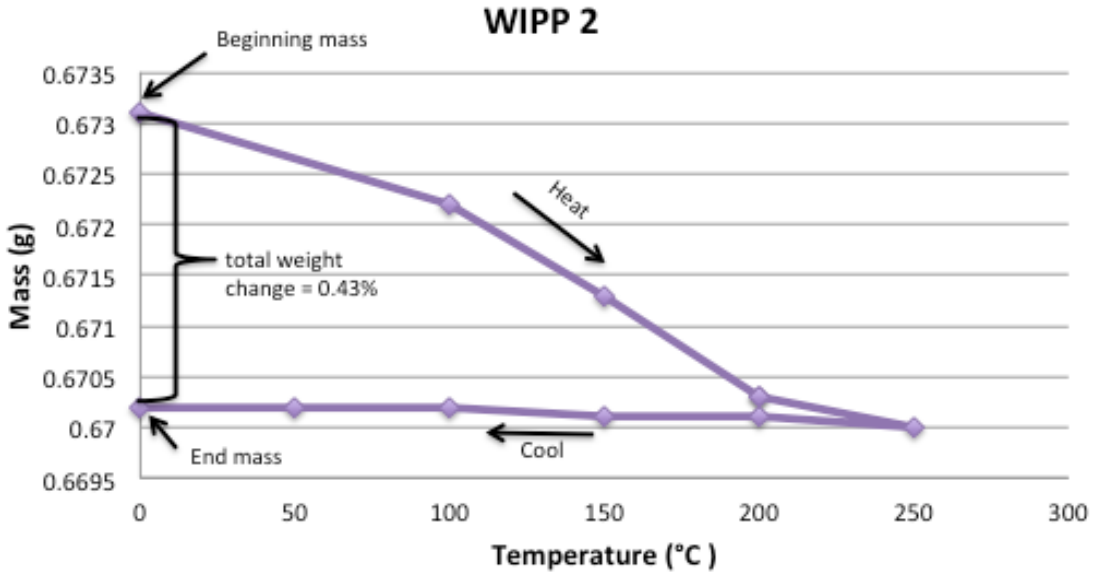

Figure B-4: Mass as a function of temperature for WIPP sample 2 showing total weight loss.

B.4.2. PHOTOMICROGRAPHS

The following photomicrographs (Tables B1-B7) represent locations in samples that experienced the most signification amount of change with respect to heating and cooling. Table 7 shows migrating fluid inclusions in the highly mineralized cleavage chip.

B.4.2.1 AVERY ISLAND SAMPLES

Table B-1: Photomicrographs for Avery Island sample 1 location 1 showing effects of heating to fluid inclusions.

Sample 1 Location 1	
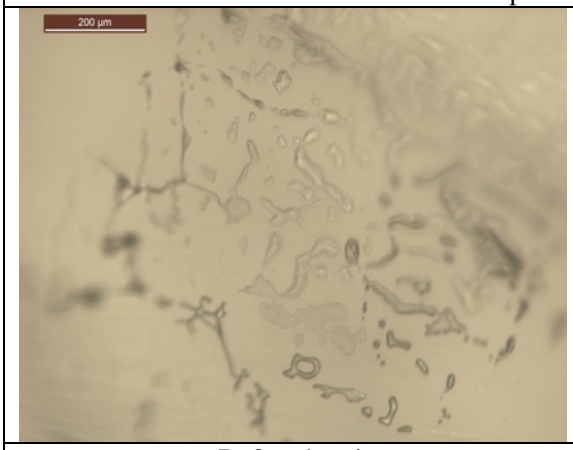	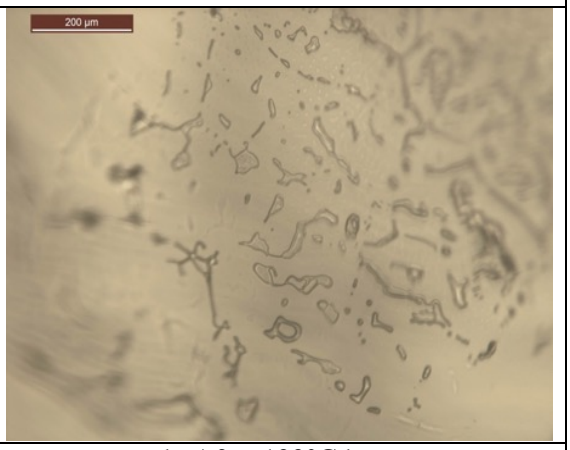
a. Before heating	b. After 100°C heat

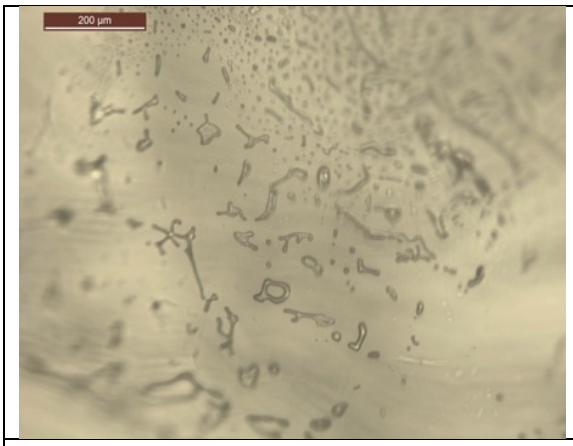

c. After 150°C heat

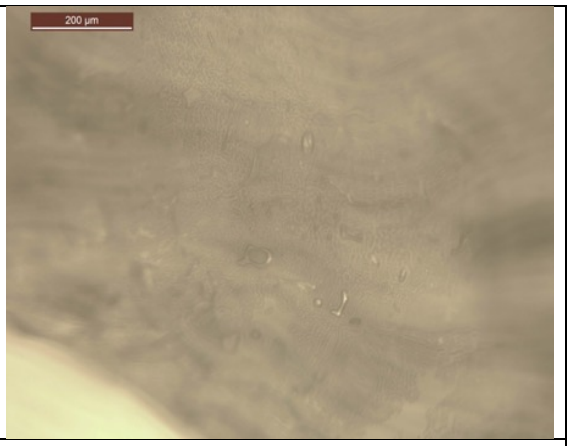

d. After 200°C heat

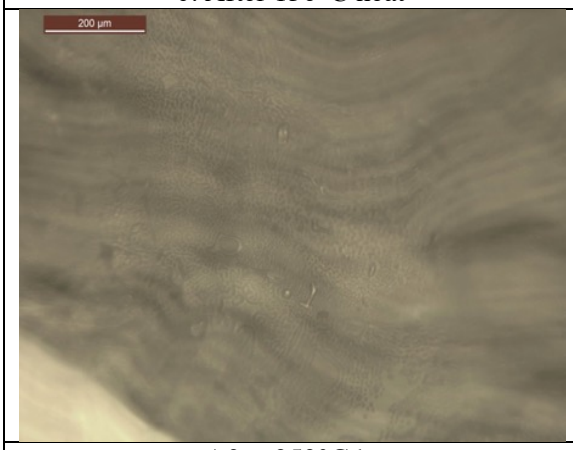

e. After 250°C heat

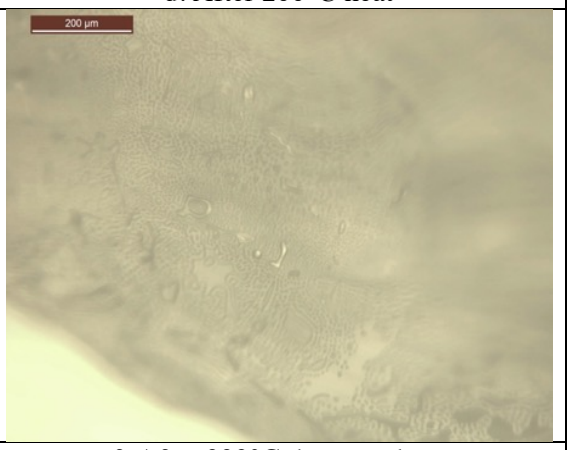

f. After 200°C decrease heat

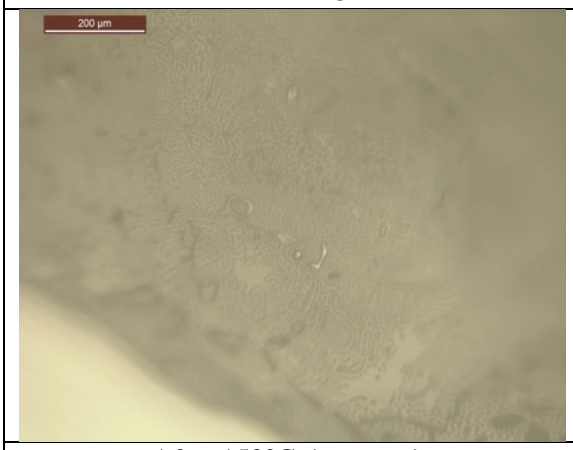

g. After 150°C decrease heat

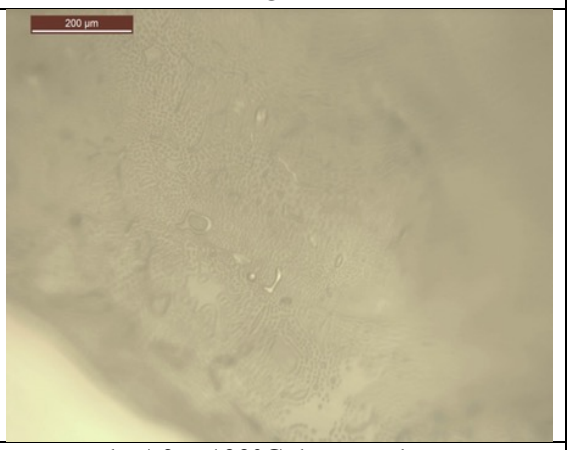

h. After 100°C decrease heat

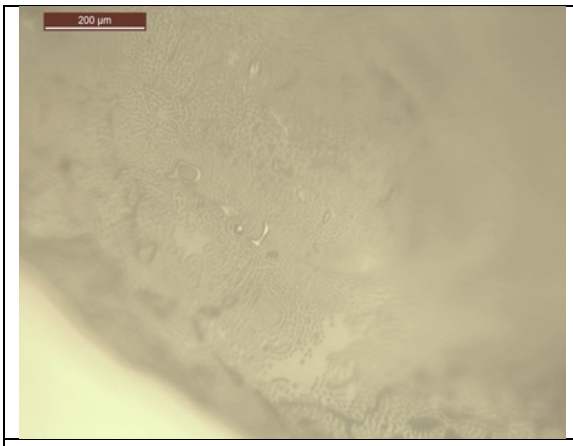	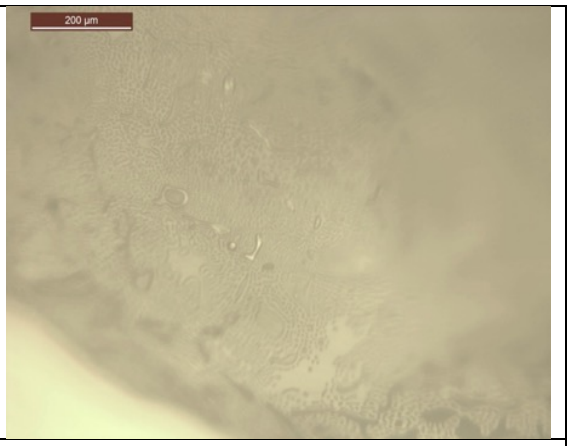
i. After 50°C decrease heat	j. After 3 day cooling at ambient

Table B-2: Photomicrographs for Avery Island sample 1 location 4 showing effects of heating to fluid inclusions.

Sample 1 Location 4	
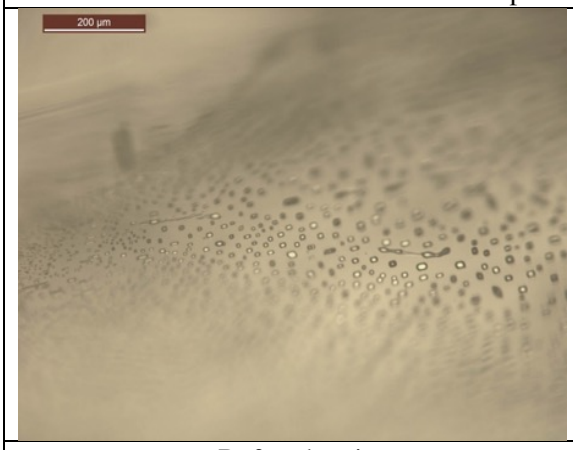	
a. Before heating	b. After 100°C heat
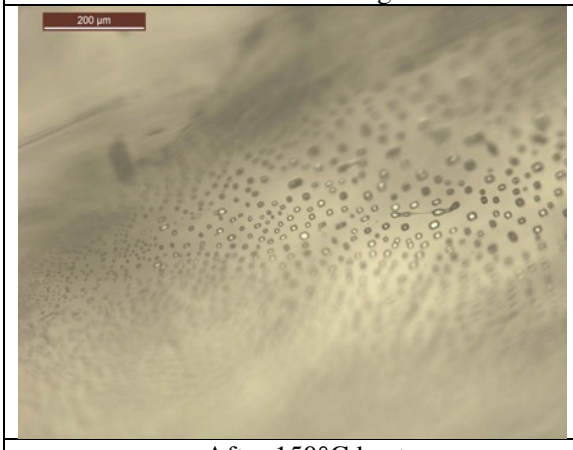	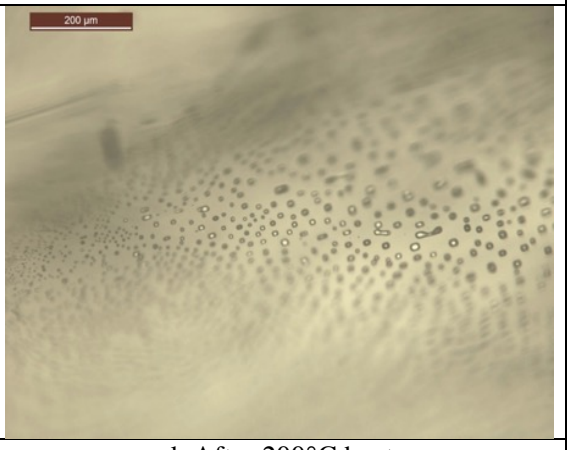
c. After 150°C heat	d. After 200°C heat

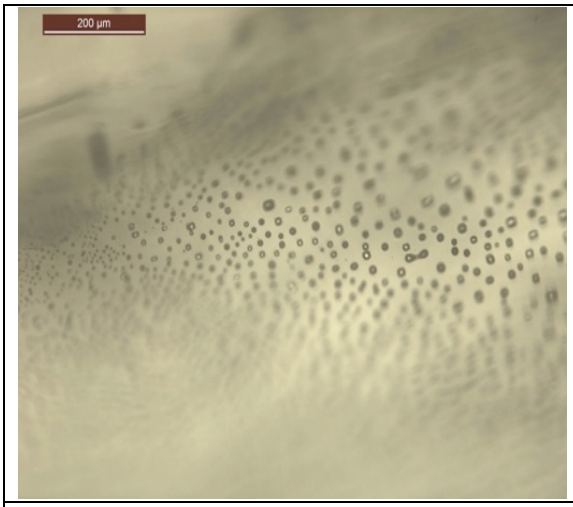	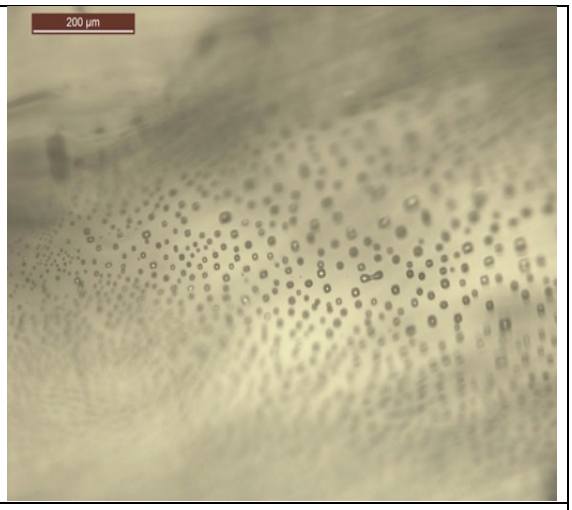
e. After 250°C heat	f. After 200°C decrease heat

Table B-3: Photomicrographs for Avery Island sample 2 location 1 showing effects of heating to fluid inclusions.

Sample 2 Location 1	
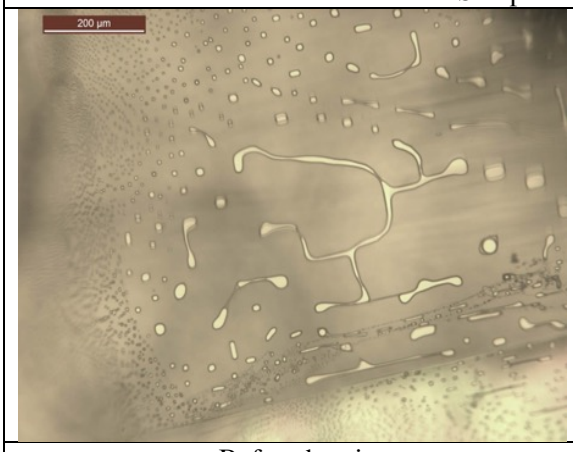	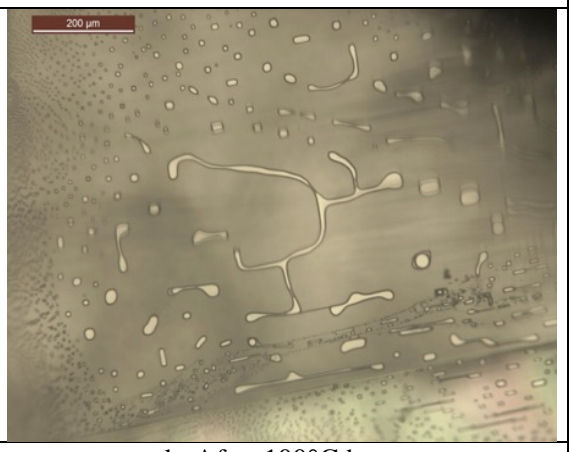
a. Before heating	b. After 100°C heat
	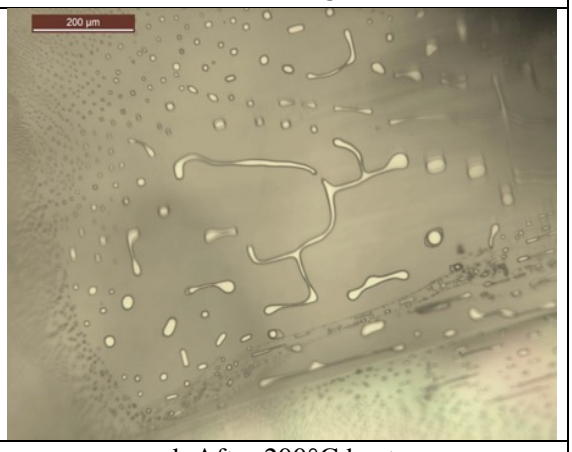
c. After 150°C heat	d. After 200°C heat

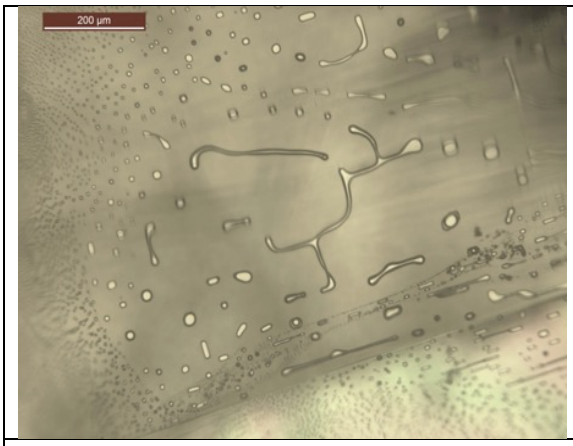

e. After 250°C heat

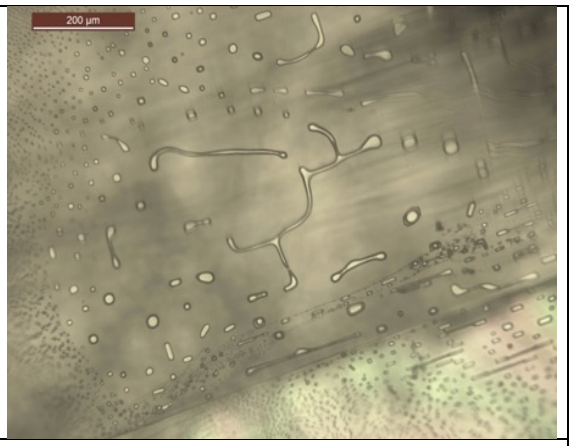

f. After 200°C decrease heat

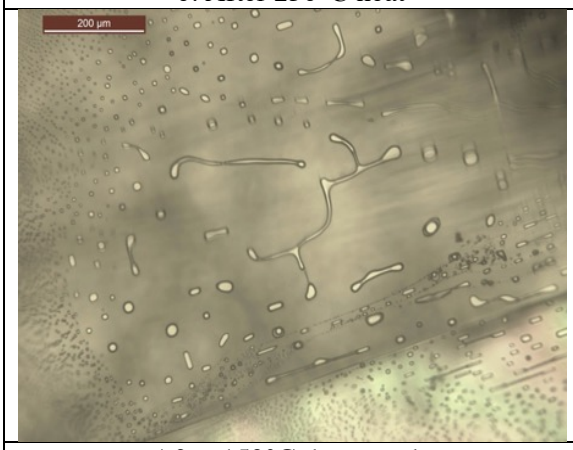

g. After 150°C decrease heat

h. After 100°C decrease heat

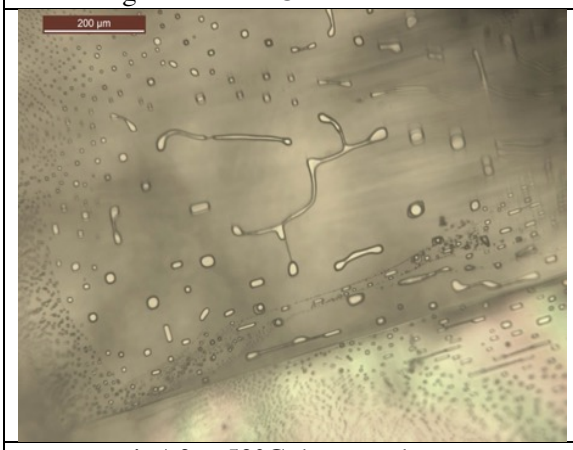

i. After 50°C decrease heat

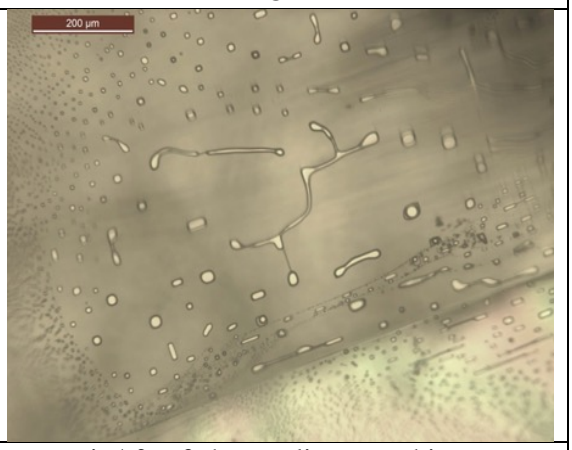

j. After 3 day cooling at ambient

B.4.4.2. WIPP SAMPLES

Table B-4: Photomicrographs for WIPP sample 1 location 3 showing effects of heating to fluid inclusions.

Sample 1 Location 3	
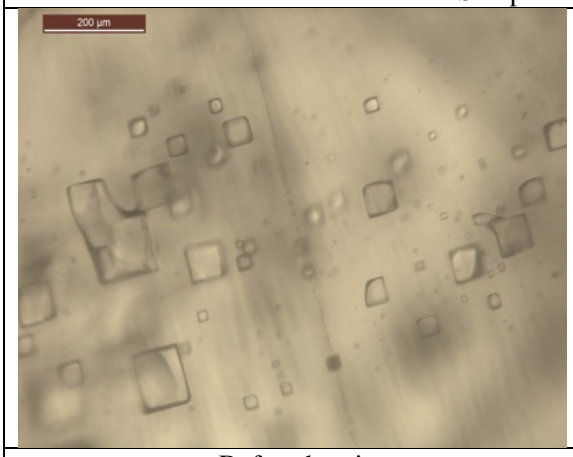	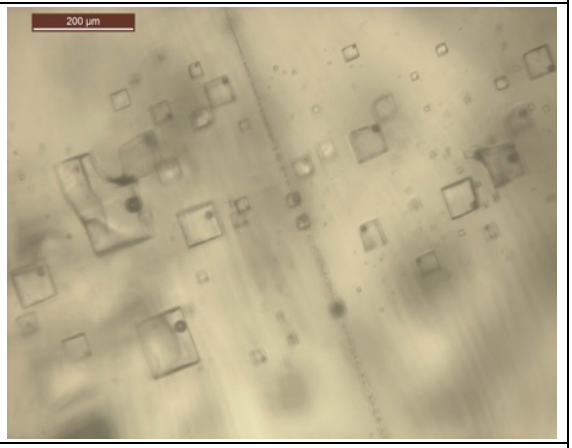
a. Before heating	b. After 100°C heat
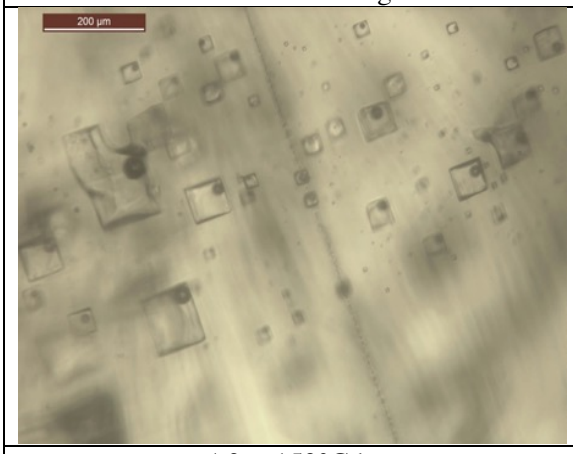	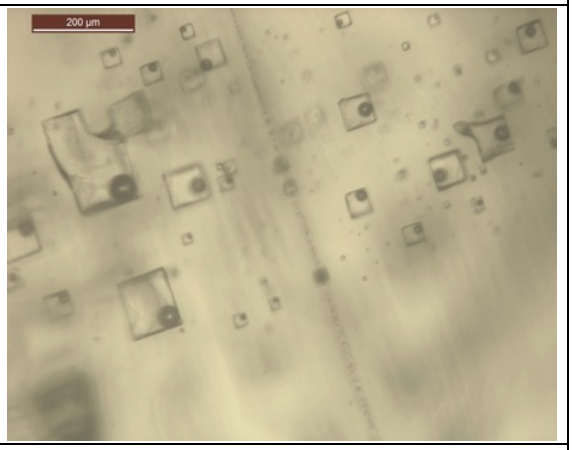
c. After 150°C heat	d. After 200°C heat
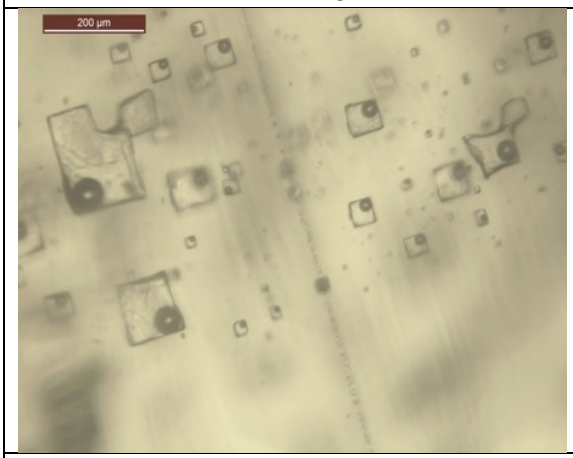	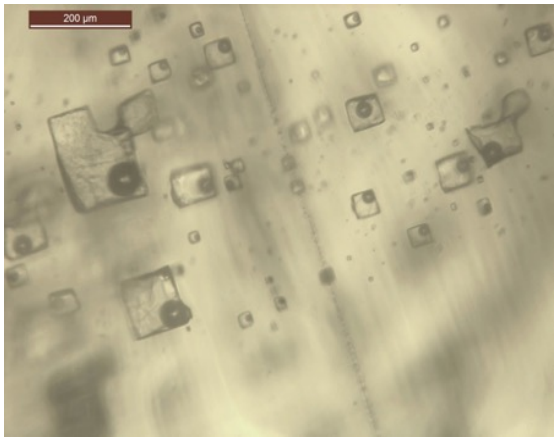
e. After 250°C heat	f. After 200°C decrease heat

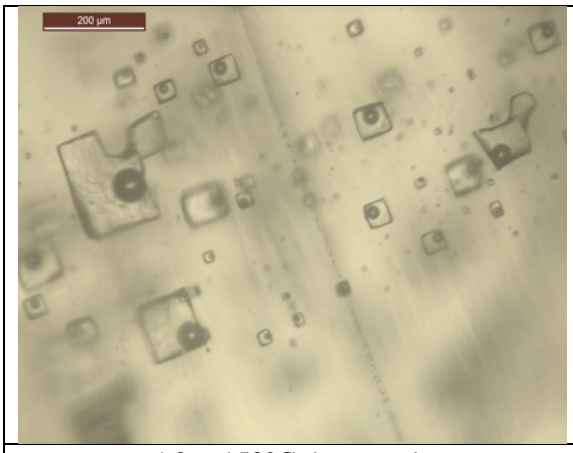	
g. After 150°C decrease heat	h. After 100°C decrease heat
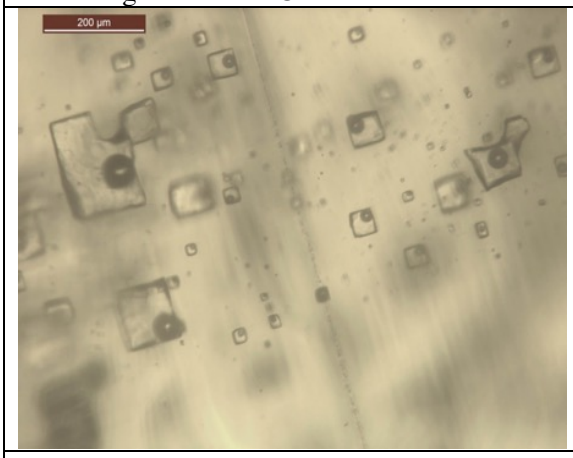	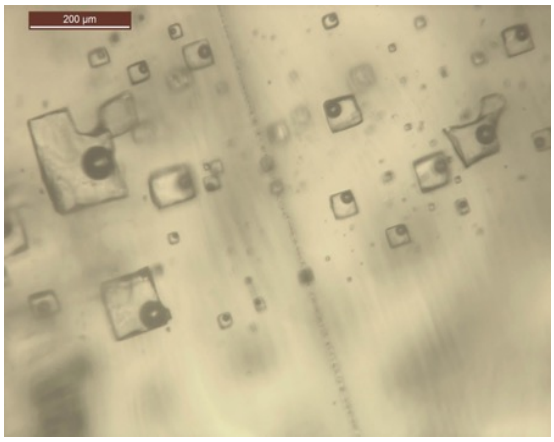
i. After 50°C decrease heat	j. After 3 day cooling at ambient

Table B-5: Photomicrographs for WIPP sample 1 location 4 showing effects of heating to fluid inclusions.

Sample 1 Location 4	
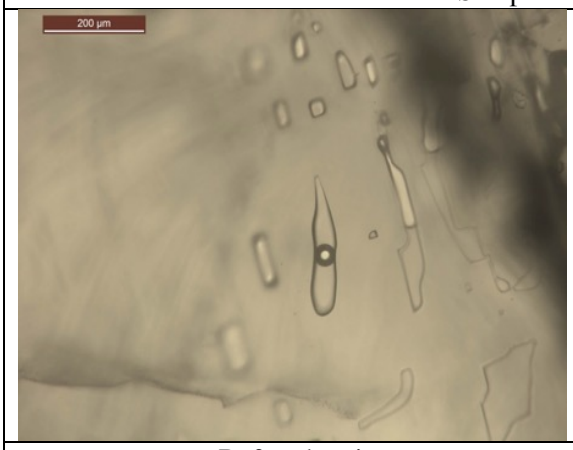	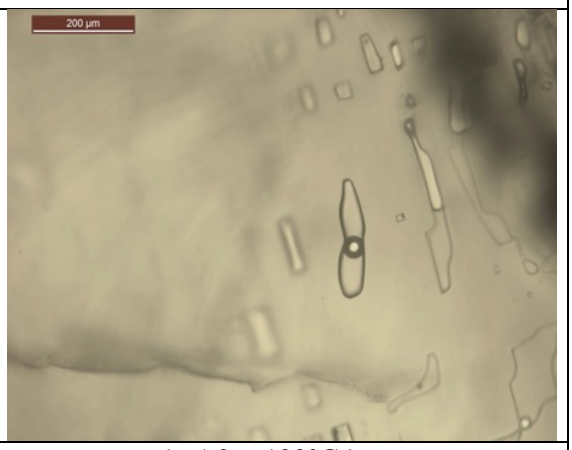
a. Before heating	b. After 100°C heat
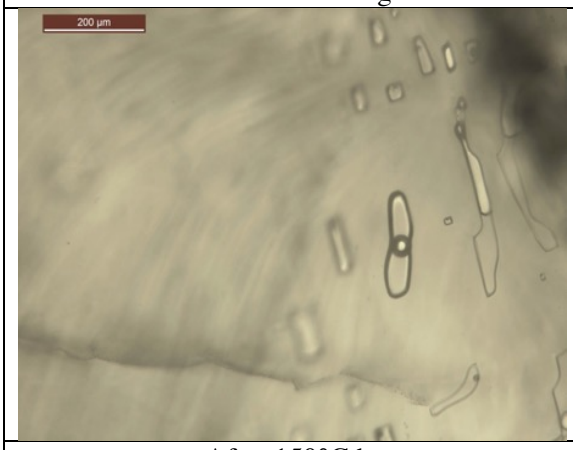	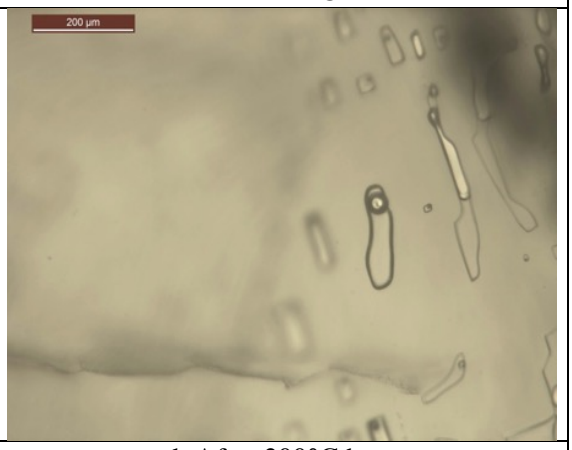
c. After 150°C heat	d. After 200°C heat
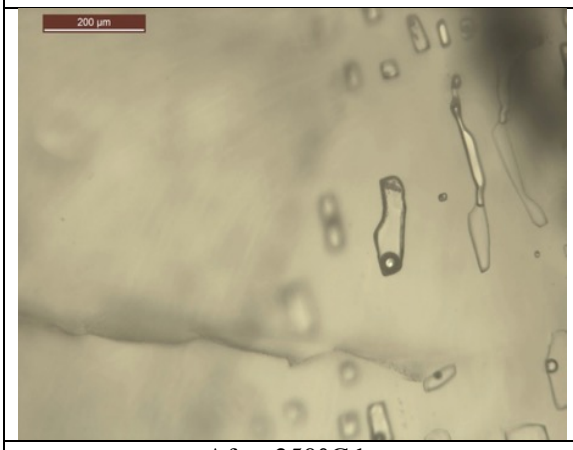	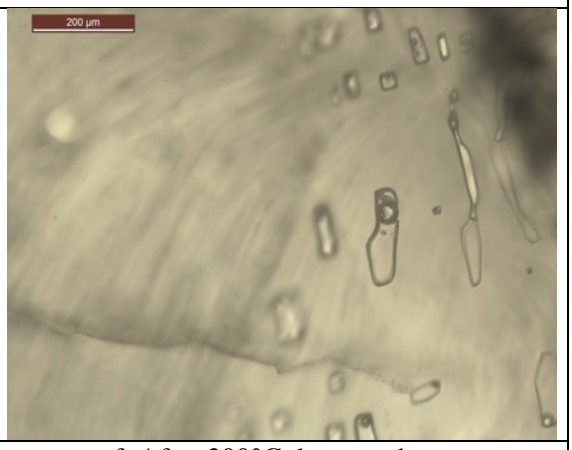
e. After 250°C heat	f. After 200°C decrease heat

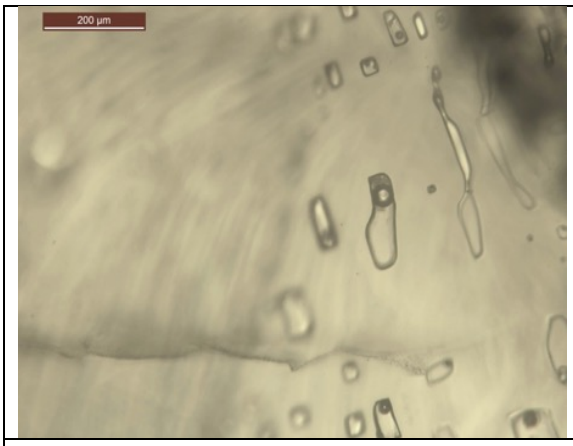	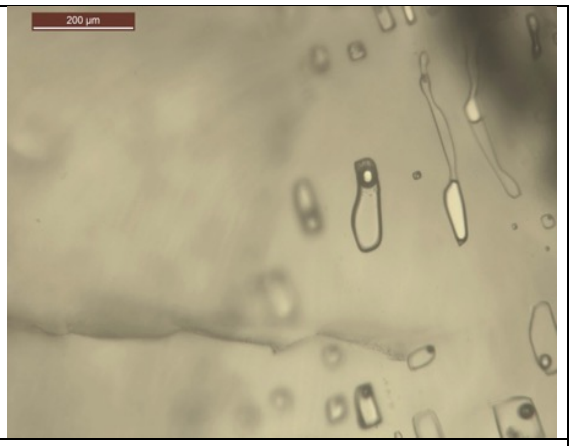
g. After 150°C decrease heat	h. After 100°C decrease heat
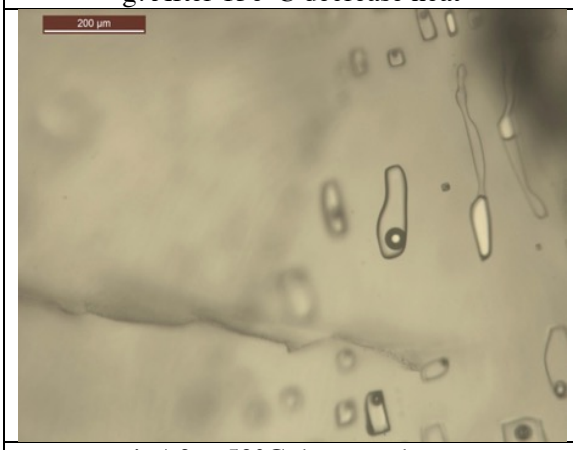	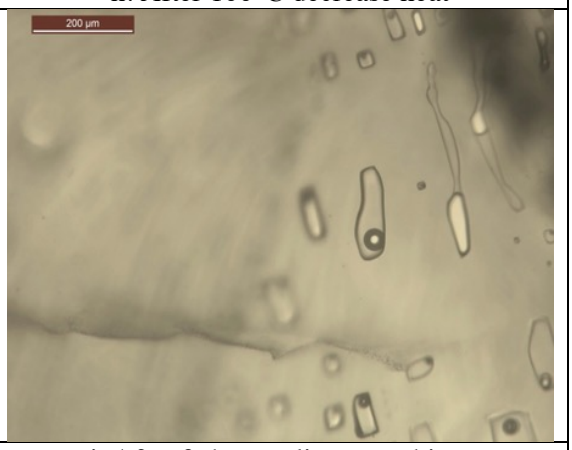
i. After 50°C decrease heat	j. After 3 day cooling at ambient

Table B-6: Photomicrographs for WIPP sample 2 location 3 showing effects of heating to fluid inclusions.

Sample 2 Location 3	
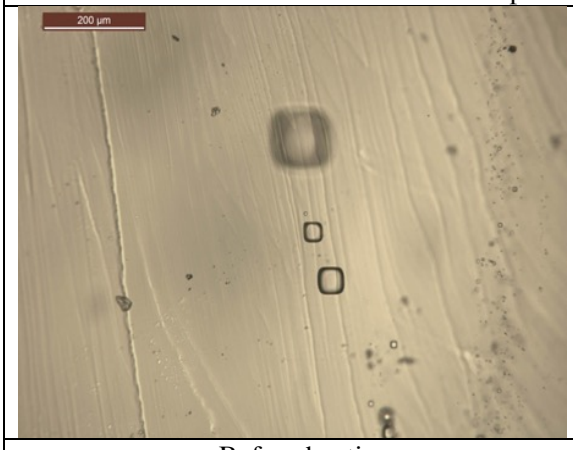	
a. Before heating	b. After 100°C heat

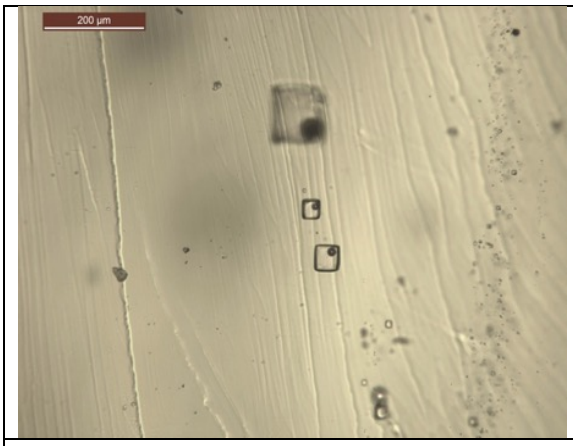

c. After 150°C heat

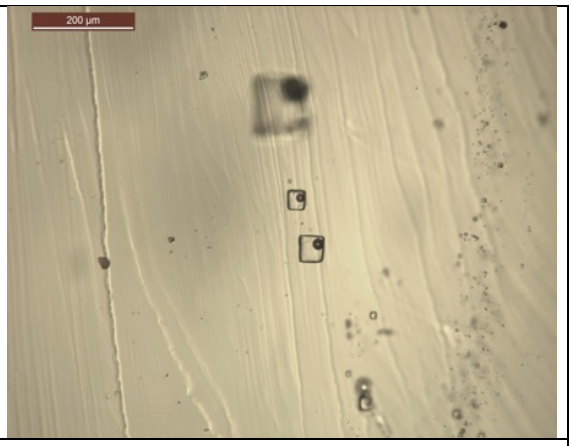

d. After 200°C heat

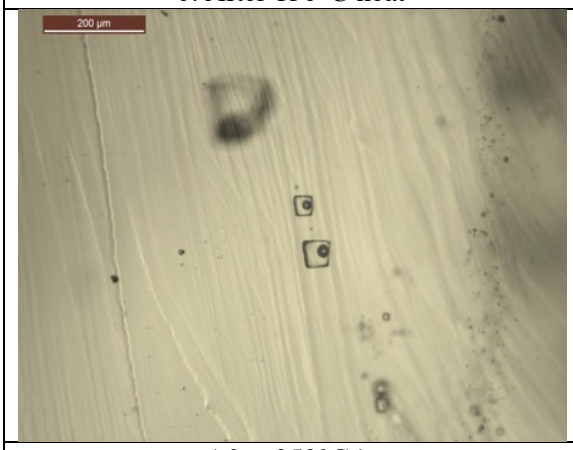

e. After 250°C heat

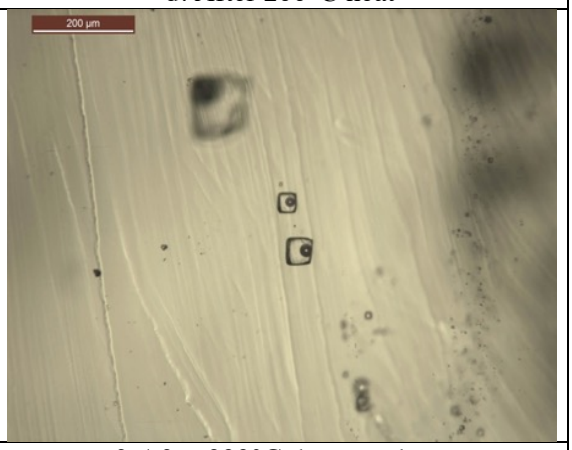

f. After 200°C decrease heat

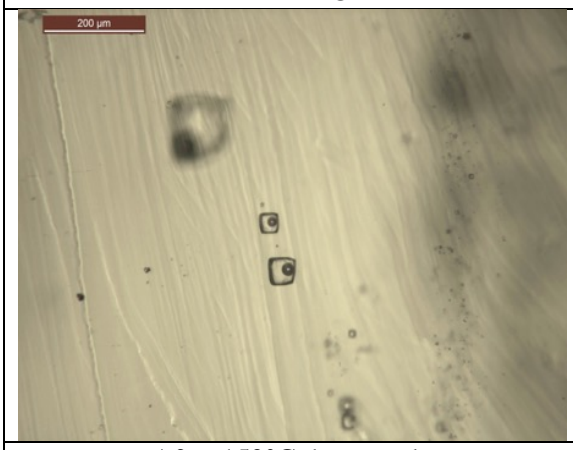

g. After 150°C decrease heat

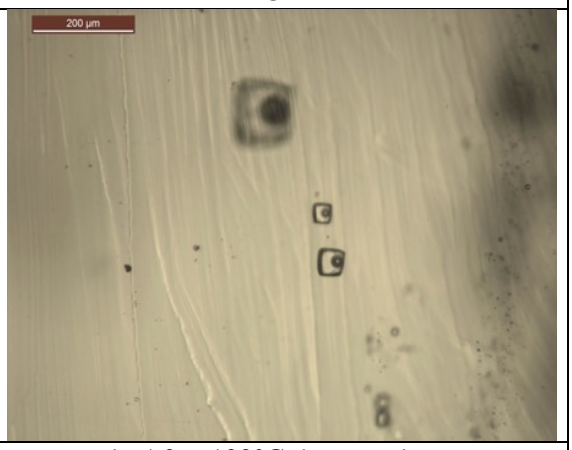

h. After 100°C decrease heat

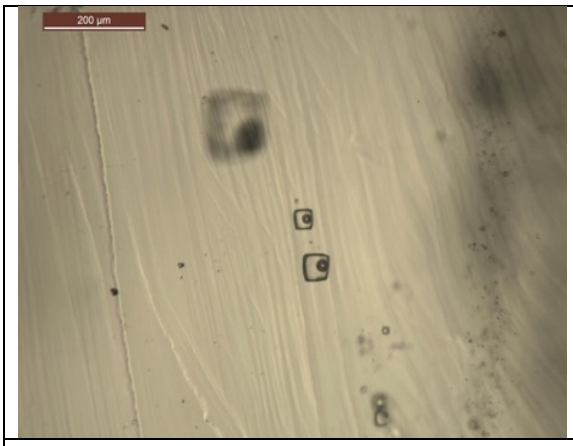	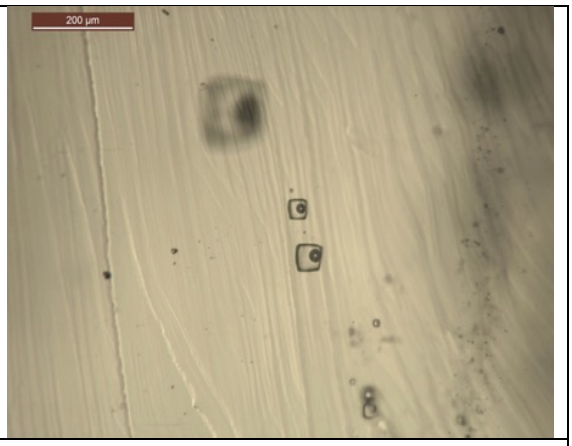
i. After 50°C decrease heat	j. After 3 day cooling at ambient

Table B-7: Photomicrographs for WIPP sample 2 at various locations near impurities showing effects of heating to fluid inclusions.

Sample 2: Migrating Fluid Inclusions After Heating	
	
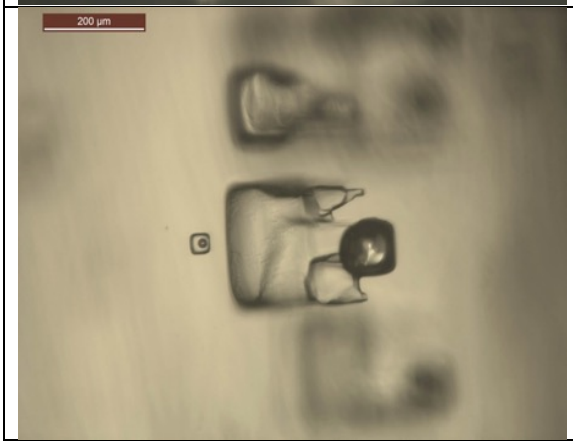	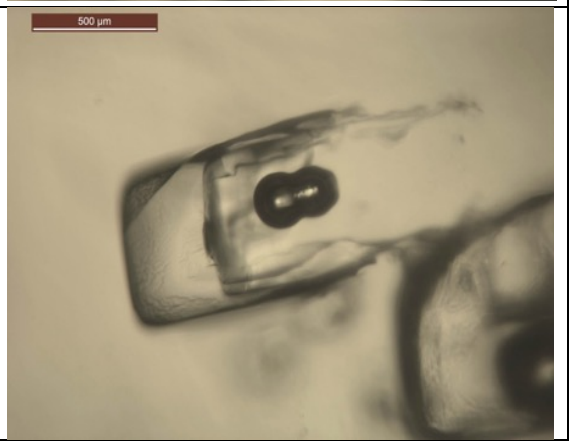

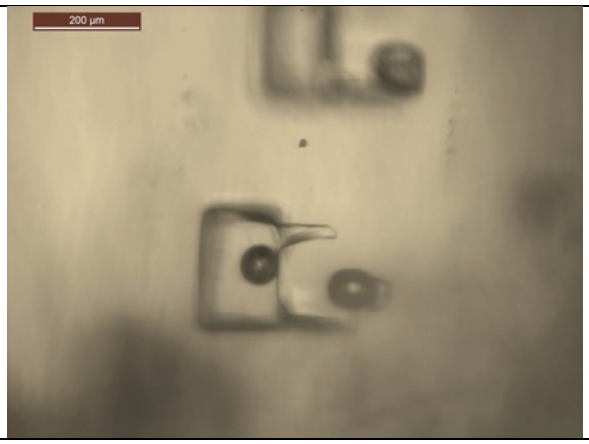

B.5. DISCUSSION

Each sample heated had at slight amount of weight change, especially the sample with a large quantity of impurities or minerals (WIPP 2, Figure B-4). The minerals attain more accessible water, which allows for higher evaporation and thus a larger weight change. Due to the small mass of each cleavage chip, a higher error is associated with the weight measurement. Higher weights may be due to dust or small particles within the convective oven that can gather in the weigh boats that are open for evaporation. As cleavage chips are transferred to the microscope stage for observation, small broken fragments may occur due to the brittle behavior of rock salt, which could also result in mass errors. These reasons could explain the inconsistent jumps in the mass loss graphs (Figures B1-B4).

From this experiment, it is clear that heat affects fluid inclusions in salt crystals. Heating the cleavage chips creates gas bubbles within many of the fluid inclusions, which did not disappear upon decreasing heat or cooling. It is predicted that this gas bubble forms due to the increase in temperature, which simultaneously produces a higher vapor pressure within the inclusion. As can be seen in tables B-4 and B-5, a rising temperature continues to make the gas bubble stretch that causes deformation or shape altering of the fluid inclusions. A very interesting observation was made in the cleavage chip with impurities, shown in photomicrographs from table B-7. A highly mineralized area, which has a higher heat capacity than pure salt, is to the right of each photomicrograph. The large fluid inclusions close to this area appear to have migrated away from this area. It is unclear as to why exactly this happens since inclusions generally move towards the heat source. More experiments need to be conducted on impure cleavage chips to see if reproducible observation can be made. It may also be important to define the type of mineral associated with each chip to determine the minerals' thermal storage properties.

APPENDIX C: OBSERVATIONAL STUDIES FROM BAMBUS II EXPERIMENT

C.1. BACKGROUND

Additional samples from the Backfilling and Sealing of Underground Repositories for Radioactive Waste in Salt (BAMBUS) field experiment (Bechthold et al. 2004) were microscopically examined by the same experimental techniques described. The BAMBUS experiment was an in situ investigation within the Asse salt mine in Germany. While the field experiment involved multiple research initiatives the samples obtained were from the Thermal Simulation of Drift Emplacement (TSDE) portion. TSDE comprised of large electric heaters placed in mined drifts, surrounded by salt backfill material, and heated to about 100°C from September 1990 to February 1999. The BAMBUS I project examined the placed backfill just after the heaters were turned off. The crushed salt backfill associated with the BAMBUS forensic work has now experienced another decade of consolidation in the underground setting. Collaborators in international salt repository investigations agreed that another series of characterization studies on the BAMBUS reconsolidated salt would help elucidate large-scale, long-term consolidation processes.

C.2. MICROSTRUCTURAL OBSERVATIONS

Fragments can be obtained several ways. Part of observational studies of reconsolidated salt involves use of a "fresh face" that has not been cut or polished. Usually fragments from cut ends can simply be broken by flexure. This exposes a clean surface, which exhibits diagnostics of sample cohesiveness, grain boundary characteristics, and other evidence of microprocesses. The SEM is convenient for these observations because of its focal length. Fragments provide a sense of 3-D imaging, particularly useful for examining grain boundaries.

Scanning electron microscopy of fragments allows close examination of grain-to-grain interaction, a general 3-dimensional appreciation of the void space, and characteristics of consolidation processes. Eight images are shown in Figure C-1 and labeled A-H. There are four micrographs for each borehole. Five images are shot at 350X magnification (~250 μm across the field of view) and the remaining three are at higher magnification to examine a few fine features of interest. A scale bar appears on each image.

Four representative images are provided from each borehole. We did not attempt to provide equal or statistical sampling, but rather to capture representative physical processes.

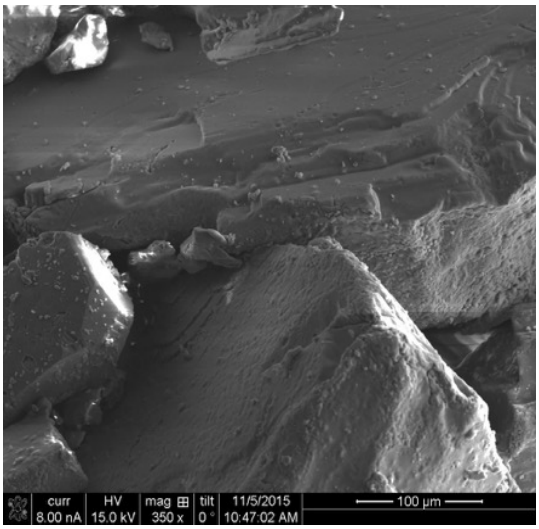

BH2-2.5m-B1_01 (A)

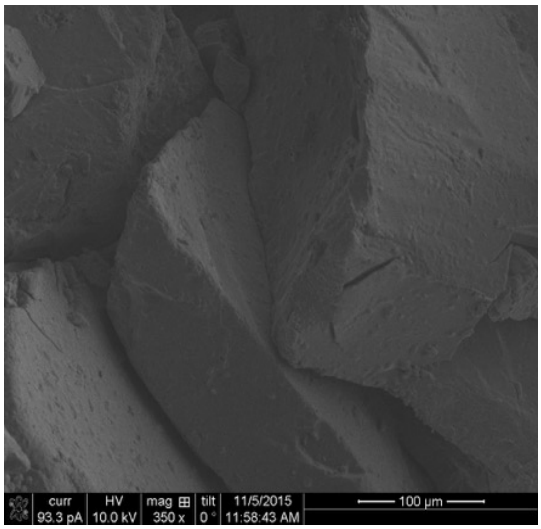

BH2-HD-A_02 (B)

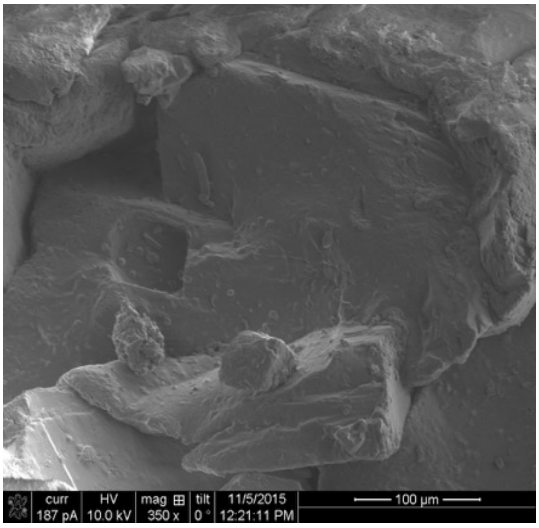

BH2-HD-A_04 (C)

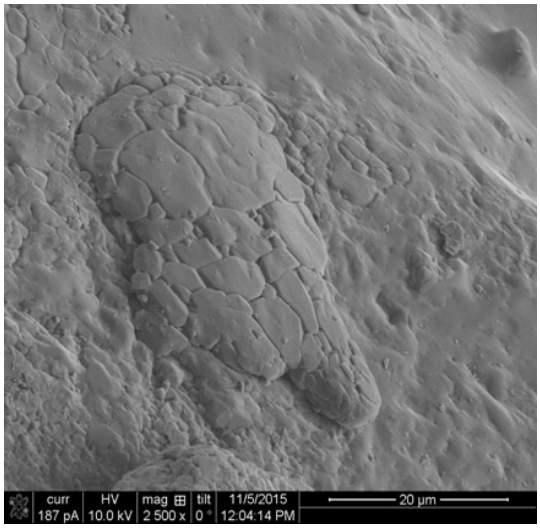

BH2-HD-A_03 (D)

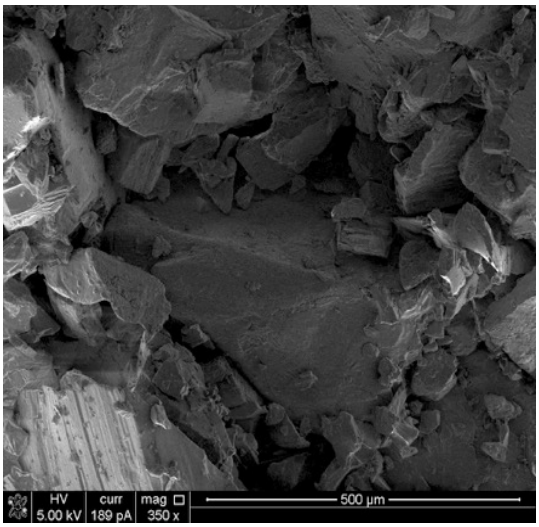

BH1-1.82m-A1_1 (E)

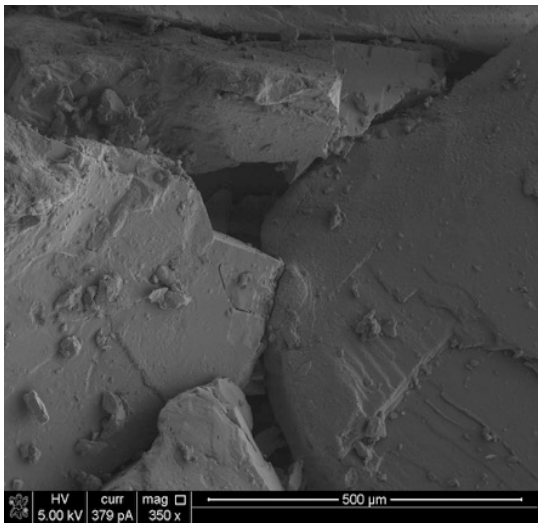

BH1-2.77m-A1_2 (F)

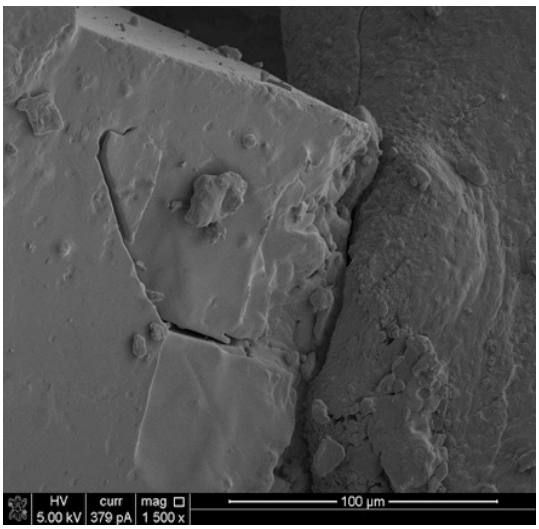

BH1-2.77m-A1_3 (G)

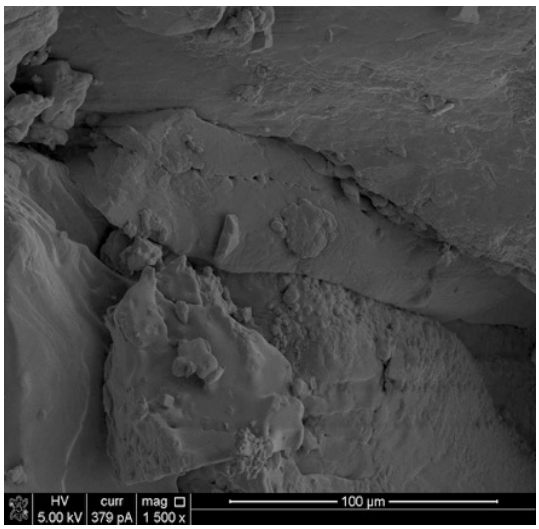

BH1-2.77m-A1_4 (H)

Figure C-1: Scanning electron images of BAMBUS salt.

A, B, and **C** are shot at 350X magnification and illustrate angular voids preserved between grain contacts. Abrasion roughens grain surfaces and is seen on most grain boundaries. The compacted mass has established relatively tight grain boundaries created by translational sliding, as exhibited in micrograph **B**. Local crystal plasticity can be seen in micrograph **C**. No suturing by fluid assisted processes is evident at 350X; however, micrograph **D** at 2500X captures a small-scale cohesion mass of fine grains within a boundary looking approximately normal to the plane.

Micrograph **E** is an example of a fragile fragment face with notably higher porosity and loose aggregate. Micrograph **F** is comparable to **A** in terms of porosity and void architecture, but also captures images of plasticity and incipient fracture at the grain contact near the center of the frame. This image is enhanced in micrograph **G**, where fracture is

developing in the left grain and plastic ridges are piling up on the right grains. Micrograph **H** illustrates tight compaction with gouge along the upper boundary of the elongate grain in the center of the field of view. Again, there is minimal evidence for fluid-aided grain-boundary processes. The level of consolidation by mostly brittle translational compaction varies considerably as will be reflected subsequently in porosity measurements.

C.3. POINT COUNTING MEASUREMENTS

We made a series of optical slides referred to as *thick-thin* sections. This oxymoronic nomenclature differentiates salt sections prepared at a thickness of 3 mm from typical rock petrographic sections that are 30 μm thick. These sections all derive from the small (bis end) piece from borehole 2 identified as BH2-HD-A. The thick-thin sections are identified in table C-1. An optical image of one of these thick-thin sections is shown in Figure C-2. Slides such as shown in FigureC-2 were used to systematically point count solid grains and void space. Porosities measured are in general agreement and compare globally to values determined by other methods. As a matter of accuracy and data quality, we performed independent measurements on the same sections and the results are summarized in table C-1. The results combine natural variability of porosity and interpretations of the operator. When independent operators counted the same slides (BH-D3 and BH-D4), average porosity was within 2%. It might be possible to reduce variance by substantially more point counting, but such measures have not been undertaken.

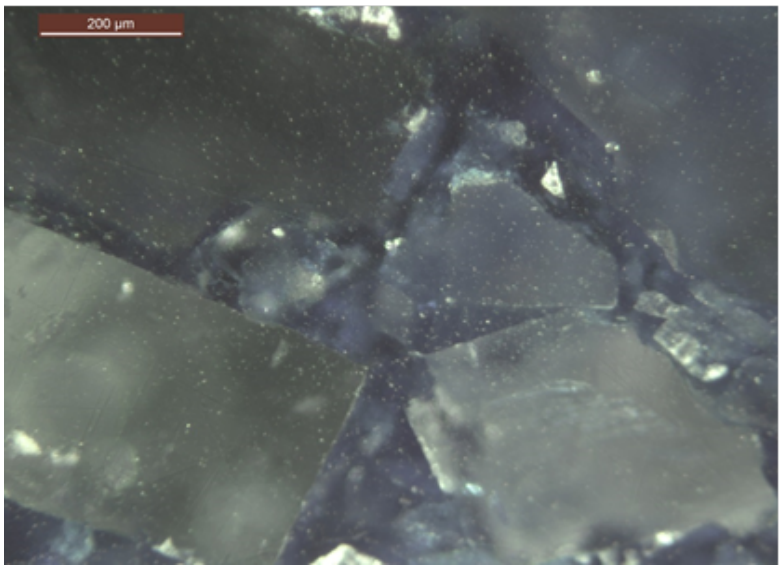

Figure C-2: Typical thick-thin section of BAMBUS reconsolidated salt (10x magnification).

Table C-1: Comparison of porosity determined by point counting.

Thin Section Identification	Voids/Hansen %	Voids/Mills %
BH-D2	20.3	
BH-D3	25.0	30.7
BH-D4	28.3	26.7
BH-D5		28.3

APPENDIX D: OBSERVATIONAL STUDIES FROM PREVIOUS SANDIA NATIONAL LABS GRANULAR SALT CONSOLIDATION EXPERIMENTS

D.1. BACKGROUND

The Geomechanics group at Sandia National Labs conducted similar consolidation tests on granular WIPP salt. A complete description, test matrix, and results can be found in SAND2012-9893P: *Coupled Thermal-Hydrological-Mechanical Processes in Salt: Hot Granular Salt Consolidation, Constitutive Model, and Micromechanics* by Hansen et al. Two samples from the matrix (FCT-CS-CR-250-01 and FCT-CS-HQ-ALL-01) were used to practice techniques described and observe deformation mechanisms. FCT-CS-CR-250-01 was consolidated to 250°C at an isostatic confining pressure of 2.5MPa to a normalized fractional density of 0.86. FCT-CS-HQ-ALL-01 was also consolidated to 250°C, but at a much higher isostatic confining pressure of 20MPa to a normalized fractional density of 0.97. Samples used for observation include impregnated thin sections, cleavage chips, and freshly broken aggregate grains.

D.2. MICROSTRUCTURAL OBSERVATIONS

In Figure D-1, photomicrographs of FCT-CS-CR-250-01 are displayed.

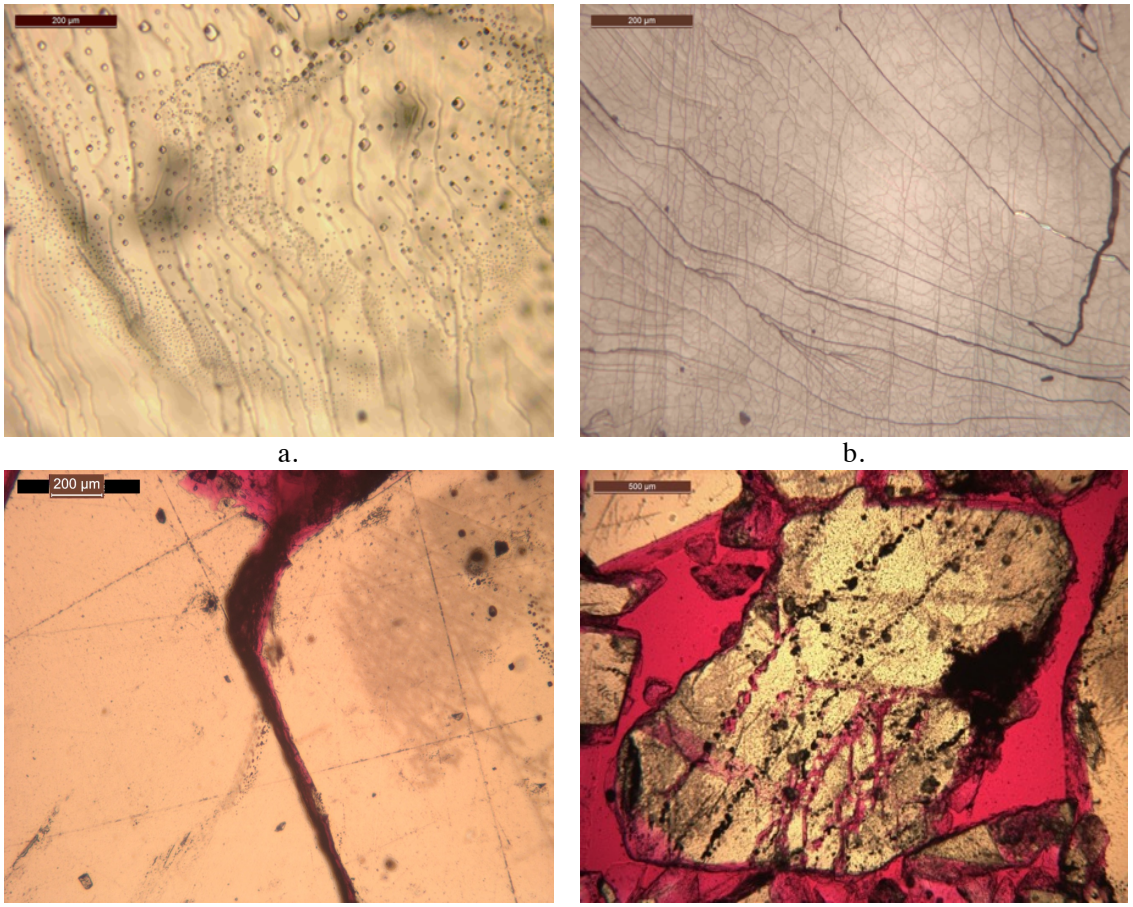

a. b.

c. d.

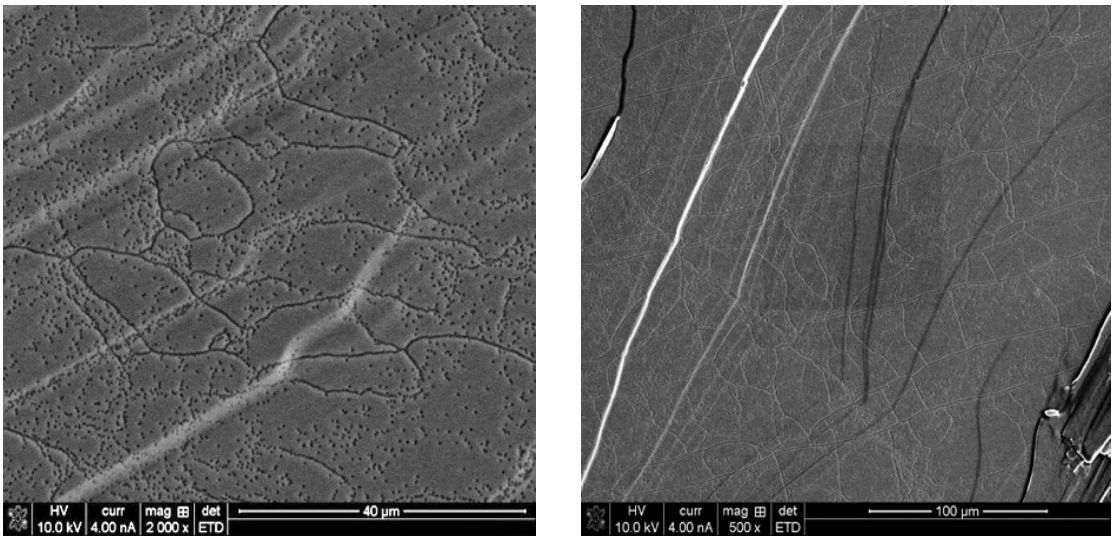

e. f.

Figure D-1: a. Cleavage chip under optical microscope showing a non-uniform array of fluid inclusions with variable sizes (10x magnification). b. Etched cleavage chip under optical microscope revealing elongated polygon substructure caused by large strain (10x magnification). c. Deformation of two cubic grains in an impregnated thin section under the optical microscope (20x magnification). d. Display of single grain under high deformation with emanating fluid inclusions (5x magnification). e. Etched cleavage chip under SEM showing low free dislocation densities with some recovered grains (2000x magnification). f. Grain in steady state due to equant polygons with very low free dislocation densities (500x magnification).

Photomicrographs of sample FCT-CS-HQ-ALL-01 are shown in Figure D-2.

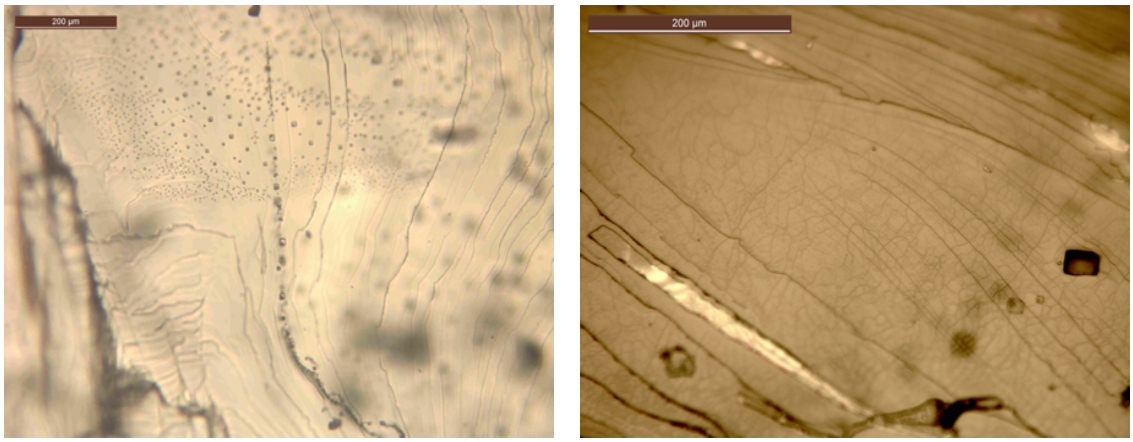

a. b.

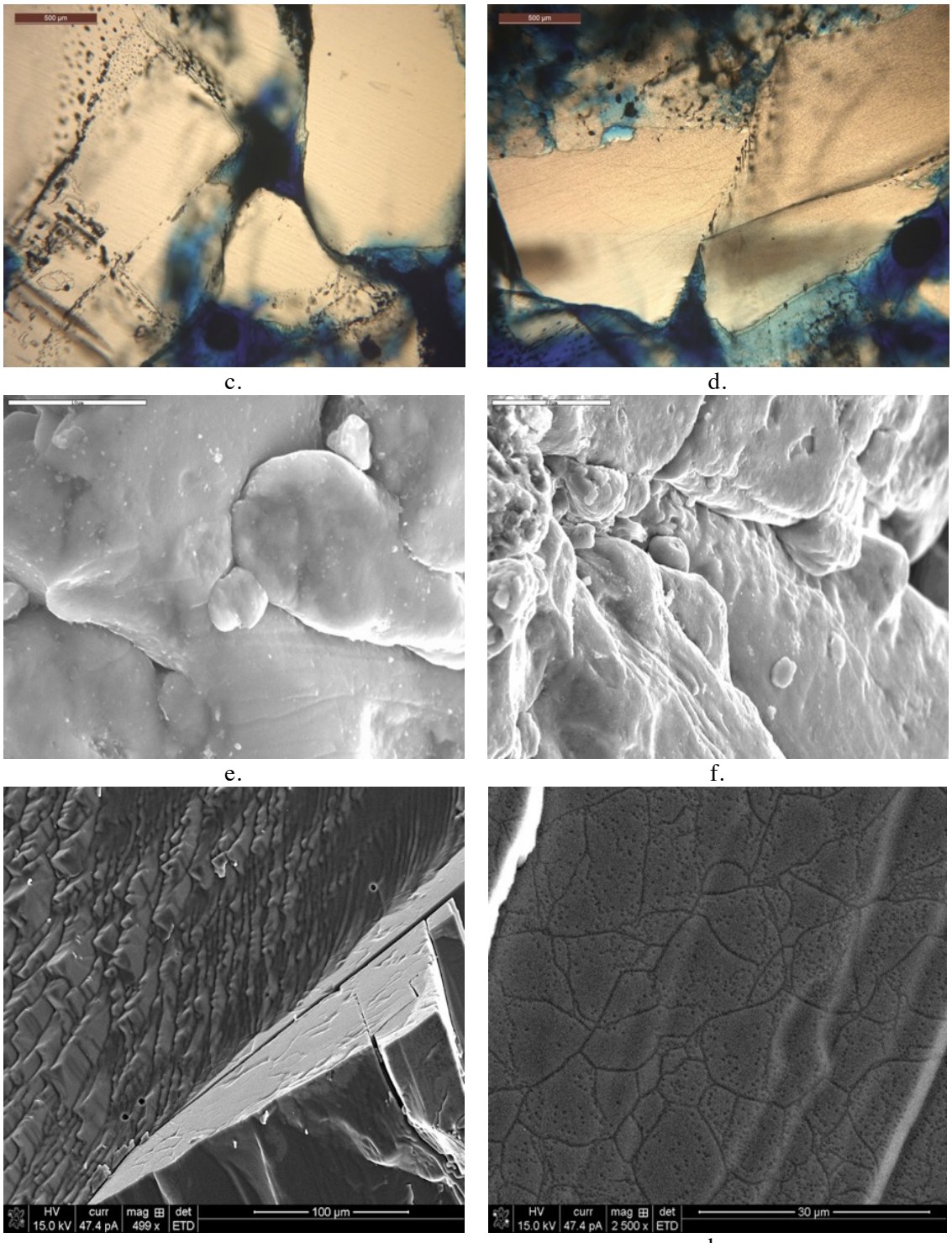

c. d. e. f. g. h.

Figure D-2: a. Cleavage chip showing more condensed and non-uniform array of variably sized fluid inclusions under optical microscope (10x magnification). b. Etched cleavage chip under optical microscope revealing elongated, smaller polygon substructure due to large strain (20x magnification). c. Small, middle grain undergoing deformation in thin section under optical microscope (5x magnification). d. Thin section showing grain under high deformation assisted by fluid inclusions (5x magnification). e. Broken aggregate under SEM revealing tight grain

boundaries with evident glide deformation (3800x magnification). f. Tightly sutured crystal deformation with plasticity by glide on broken aggregate under SEM (1600x magnification). g. Edge of cleavage chip under SEM displaying tight sutured grain boundary with upper grain under heavy deformation where glide planes are curved, and lower grain having perfect cubic cleavage on three faces (499x magnification). h. Smaller subgrain structure with lower free dislocation densities on etched cleavage chip under SEM (2500x magnification).

D.3. DISCUSSION

Between the two samples, observational results show that at different consolidating pressure affect the subgrain structure. The higher fractional density sample, FCT-CS-HQ-ALL-01, had much smaller subgrains and lower free dislocation densities when compared to the lower fractional density sample. There was also a larger degree of fluid-aided process occurring at grain boundaries. These results are consistent with previous researchers. Remarkably, the bedded granular salt used in these experiments continues to vent moisture during the consolidation. Evidently, fluid inclusion migration and hydrous mineralogy are sufficient to promote fluid aided processes at grain boundaries. Substructures mark crystal plastic processes as well as recovery.

REFERENCES

Anselmetti, F.S., Luthi, S., Eberli, G.P., 1998. Quantitative characterization of carbonate pore systems by digital image analysis. AAPG Bull. 82, 1815-1836.

Bauer, S.J., Broome, S.T., Hansen, F.D., Lampe, B., Mills, M.M., Stormont, J.C., 2015. Gas flow measurements of consolidating crushed salt. 49th US Rock Mechanics/Geomechanics Symposium, San Francisco, CA, USA.

Blanco Martin, L., Rutqvist, J., Birkholzer, J.T., 2015. Long-term modeling of the thermal–hydraulic–mechanical response of a generic salt repository for heat-generating nuclear waste. Eng. Geo. Vol. 193, 198–211.

Brodsky, N.S., 1994. Hydrostatic and shear consolidation tests with permeability measurements on Waste Isolation Pilot Plant crushed salt. SAND93–7058. Sandia National Laboratories, Albuquerque, NM.

Brodsky, N.S., Hansen, F.D., Pfeifle, T.W., 1996. Properties of dynamically compacted WIPP salt. The Mechanical Behavior of Salt IV: Proceedings of the fourth Conference, (MECASALT IV) Montreal, edited by M. Aubertin and H.R. Hardy Jr., Trans Tech Publ., Clausthal, Germany.

Broome, S.T., Bauer, S.J., Hansen, F.D., 2014. Reconsolidation of Crushed Salt to 250°C Under Hydrostatic and Shear Stress Conditions. 48th US Rock Mechanics/Geomechanics Symposium, Minneapolis, MN, USA.

Callahan, G.D., Loken, M.C., Hurtado, L.D., Hansen, F.D., 1996. Evaluation of Constitutive Models for Crushed Salt. The Mechanical Behavior of Salt IV: Proceedings of the fourth Conference, (MECASALT IV) Montreal, edited by M. Aubertin and H.R. Hardy Jr., Trans Tech Publ., Clausthal, Germany.

Callahan, G.D., Mellegard, K.D., Hansen, F.D., 1998. Constitutive Behavior of Reconsolidating Crushed Salt. Int. J. Rock Mech. Min. Sci. 35, No. 4-5, Elsevier.

Carter, N.L., Heard, H.L., 1970. Temperature and rate dependent deformation of halite. Am. J. Sci. 269, 193-249.

Carter, N.L, Hansen, F.D., Senseny, P.E., 1982. Stress magnitudes in natural rock salt. J. Geophy. Res. 87, no. B11, 9289-9300.

Case, J.B., Kelsall, P.C., Withiam, J.L., 1987. Laboratory investigation of crushed salt consolidation. 28th US Symposium on Rock Mechanics, Tucson, AZ.

Cerepi, A., Humbert, L., Burlot, R., 2001. Petrophysical properties of porous medium from Petrographic Image Analysis data. Colloids and Surfaces A: Physiochem. Eng. Aspects. Vol. 187-188, 233-256.

Cinar, Y., Pusch, G., Reitenbach, V., 2006. Petrophysical and capillary properties of compacted salt. Transport in Porous Media. 64, 199-228.

Desbois, G., Závada, P., Schléder, Z., Urai, J., 2010. Deformation and recrystallization mechanisms in actively extruding salt fountain: Microstructural evidence for a switch in deformation mechanisms with increased availability of meteoric water and decreased grain size (Qum Kuh, central Iran). J. Struct. Geo. 32, 580-594.

De Las Cuevas, C., 1997. Pore structure characterization in rock salt. Eng. Geo. Vol. 47, 17-30.

Dullien, F.A.L., 1991. Porous Media: Fluid Transport and Pore Structure, second ed. San Diego, California.

Hansen, F.D., Bauer, S.J., Broome, S.T., Callahan, G.D., 2012. Coupled thermal-hydrological-mechanical processes in salt: Hot granular salt consolidation, constitutive model and micromechanics. FCRD-UFD-2012-000422, SAND2012-9893P. Albuquerque, NM: Sandia National Laboratories.

Hansen, F.D., 2014. Micromechanics of isochoric salt deformation. 48th US Rock Mechanics/Geomechanics Symposium. Minneapolis, MN, USA. ARMA 14-7012.

Hansen, F.D., Popp, T., Wieczorek, K., Stührenberg D., 2014. Granular salt summary: Reconsolidation principles and applications. Prepared for U.S. DOE Used Fuel Disposition, SAND2014-16141R, Sandia National Laboratories, Albuquerque, NM, USA.

Hansen, F.D., Popp, T., Wieczorek, K., Stührenberg D., 2015. Salt reconsolidation applied to repository seals. 49th US Rock Mechanics Symposium, San Francisco, CA, USA.

Holcomb, D. J., Shields, M., 1987. Hydrostatic creep consolidation of crushed salt with added water. *SAND87-1990*, Sandia National Laboratories, Albuquerque, NM.

Hunsche, U., Hampel, A., 1999. Rock salt – The mechanical properties of the host rock material for a radioactive waste repository. Eng. Geo.Vol. 52, No. 3, 271-291.

Hunsche, U., Schulze, O., 2002. Humidity induced creep and it's relation to the dilatancy boundary, in Basic and Applied Salt Mechanics, 73 – 87, Swets and Zeitlinger, Lisse, Netherlands.

Keller, L.M., Jobmann, M., Schuetz, P., Gasser, P., 2014. On the potential of tomographic methods when applied to compacted crushed rock salt. Transp. Porous Med. 104, 607-620.

Kuhlman, K., 2014. Summary Results for Brine Migration Modeling Performed by LANL, LBNL, and SNL for the UFD Program, US Department of Energy Fuel Cycle Research and Development report FCRD-UFD-2014-000071, prepared by Sandia National Laboratories.

Mowers, T.T., Budd, D.A., 1996. Quantification of porosity and permeability reduction due to calcite cementation using computer-assisted pertrographic image analysis techniques. APPG Bulletin, Vol. 80, No. 3, 309-322.

Paneru, L.P., 2016. Measurement of thermal properties and porosity of consolidated salt. Master's thesis, University of New Mexico, Albuquerque, New Mexico.

Pennock, G.M., Zhang, X., Peach, C.J., Spiers, C.J., 2007. Microstructural study of reconsolidated salt, in: Wallner, M., Lux, K.H., Minkley, W., Hardy, H.R.J. (Eds.), The Mechanical Behavior of Salt – Understanding of THMC Processes in Salt: Proceedings of the 6th Conference (SaltMech6), Hannover, Germany. Taylor & Francis Group, London, pp. 149-158.

Peters, E.J., 2012. Advanced Petrophysics: Geology, Porosity, Absolute Permeability, Heterogeneity, and Geostatistics, Vol. 1, Greenleaf Book Group.

Pisani, L., 2011. Simple expression for the tortuosity of porous media. Transport in Porous Media, Vol. 88, Issue 2, 193-203.

Popp, T., Salzer, K., Spiers, C., Stuhrenberg, D., Schulze, O., Wiezcorek, K., 2013. Microstructural deformation processes in granular salt during mechanical compaction, in: Hansen, F.D., Kuhlman, K.L., Steininger, W., Biurrun, E. (Eds.), Proceedings of 3rd US/German Workshop on Salt Repository Research, Design and Operation. SAND 2013-1231P.

Schindelin, J., Arganda-Carreras, I., Frise, E., Kaynig, V., Longair, M., Pietzsch, T., Preibisch, S., Rueden, C., Saalfeld, S., Schmid, B., Tinevez, J., White, D., Hartenstein, V., Eliceiri, K., Tomancak, P., Cardona, A., 2012. Fiji: an open-source platform for biological-image analysis, Nature Methods 9, 676-682.

Schléder, Z., Urai, J.L., 2005. Microstructural evolution of deformation- modified primary halite from Hengelo, the Netherlands. Int. J. Earth Sci., 94(5-6), 941-956.

Senseny, P.E., Hansen F.D., Russell, J.E., Carter, N.L., Handin, J.W., 1992. Mechanical behavior of rock salt: Phenomenology and micromechanisms. Int. J. Rock Mech. Min. Sci. & Geomech., Vol. 29, Iss. 4, 363-378.

Spiers, C.J., Brzesowsky, R.H., 1993. Densification behavior of wet granular salt: theory versus experiment. Seventh Symposium on Salt, Vol. I. Elsevier Science Publishers, B.V., Amsterdam.

Spiers, C.J., Schutjens, P.M.T.M., Brzesowsky, R.H., Peach, C.H., Liezenberg, J.L., Zwart, H.J., 1990. Experimental determination of constitutive parameters governing creep of rocksalt by pressure solution, in: R.J. Knipe and E.H. Rutter (Eds), Deformation Mechanisms, Rheology and Tectonics. Geological Society, London, Spec. Publ., 54, pp. 215-227.

Stormont, J.C., Lampe, B., Mills, M., Paneru, L., Lynn, T., 2015. Observations of permeability changes from granular salt consolidation, NEUP project 13-4834 report, prepared by the University of New Mexico for the US Department of Energy, July 15.

Stührenberg, D., Schulze, O., 2012. Porosity and permeability of crushed and damaged rock salt during compaction, in: Bérest, P., Ghoreychi, M., Hadj-Hassen, F., Tijani, M. (Eds.), Mechanical Behavior of Salt VII. Taylor & Francis Group, London, pp. 275-282.

Underwood, E.E., 1980. Stereological analysis of particle characteristics, in: Beddow, J.K., Meloy, T. (Eds.), Testing and Characterization of Powders and Fine Particles, Heyden, London.

Urai, J.L., Spiers, C.J., 2007. The effect of grain boundary water on deformation mehanisms and rheology of rocksalt during long-term deformation, in: Wallner, M., Lux, K.H., Minkley, W., Hardy, H.R.J. (Eds.), The Mechanical Behavior of Salt – Understanding of THMC Processes in Salt: Proceedings of the 6th Conference (SaltMech6), Hannover, Germany. Taylor & Francis Group, London, pp. 149-158.

Urai, J.L., Means, W.D., Lister, G.S., 1986a. Dynamic recrystallization of minerals, in: Hobbs, B.E., Heard, H.C. (Eds), Mineral and Rock Deformation: Laboratory Studies– The Paterson Volume. AGU Geophysical Monograph 36, pp. 161-199.

Urai, J., Spiers, C., Zwart, H., Lister, G., 1986b. Weakening of rock salt by water during long-term creep. Nature 324, 554-557.

Winterle, J., Ofoegbu, G., Pabalan, R., Manepally, C., Mintz, T., Pearcy, E., Smart, K., McMurry, J., Pauline, R., Fedors, R., 2012. Geologic disposal of high-level radioactive waste in salt formations. Prepared for U.S. Nuclear Regulatory Commission Contract NRC-02-07-006.

Zhu, C., Jeong, S.H., Dutta, M., Arson, C., 2015. Image Processing of Fabric Evolution in Granular Salt subject to Diffusive Mass Transfer, Mechanical Behavior of Salt VIII, Rapid City, South Dakota, 26-28 May 2015.

Zhu, W., David, C., Wong, T., 1994. Network modeling of permeability evolution during cementation and hot isostatic pressing. J. Geophy. Res. 100, No. B8, 15,451-15,464.